FACULDADE DE ENGENHARIA DA UNIVERSIDADE DO PORTO

# Evaluation of Stall Behavior of a Slotted Airfoil at Low Reynolds Numbers

**Cindy Zozimo Aranda de Almeida**

U.PORTO

FEUP FACULDADE DE ENGENHARIA UNIVERSIDADE DO PORTO

Master of Science in Computational Mechanics

Supervisor: Dr. José César de Sá

July 10, 2023

# Evaluation of Stall Behavior of a Slotted Airfoil at Low Reynolds Numbers

**Cindy Zozimo Aranda de Almeida**

Master of Science in Computational Mechanics

July 10, 2023

# Abstract

Stall occurs in an airfoil when it reaches a critical angle of attack and the flow detaches from its surface, causes a sudden reduction in lift coefficient values. Several mechanisms have been studied and applied to aircraft to mitigate this phenomenon in the intermediate and high Reynolds number flow regimes, where the flow is governed by inertial forces. In the low Reynolds number regime, the flow is governed by viscous forces, and stall mechanisms need to be studied to effectively implement countermeasures in this regime. This thesis evaluates the slotted blade design developed by [1], by performing 2D CFD (Computational Fluid Dynamics) simulations to observe fluid behavior at Reynolds number $10^4$. Results showed that the slotted design delays boundary layer separation, mitigates the stall angle for the NACA 0015 airfoil from $12^\circ$ to $18^\circ$, and the flow presents smaller variation in lift and drag coefficients.

[1] Zao Ni [1]

# Acknowledgements

I would like to thank my dad for his input and discussions over the years. Thanks to my friends, home and abroad, for all the support over the years. It was fun.

Special thanks to Dr. Meilin Yu, without whom I wouldn't have been able to explore the aerodynamics field or acquire a liking for, and Dr. Naresh Poudel for his guidance and patience.

Thanks to my advisor Dr. César de Sá for his advice and Dr. Marco Parente for his technical support throughout my masters.

Thanks to Ben Kale for his input and long discussions which made this thesis pleasant to read.

Cindy Almeida

*“You should be glad that bridge fell down.*
*I was planning to build thirteen more to that same design”*

Isambard Kingdom Brunel

# Contents

# List of Figures

# Abbreviations and symbols

| | |
|---|---|
| AoA | Angle of attack |
| CFD | Computational Fluid Dynamics |
| ESDIRK | Explicit singly diagonal implicit Runge-Kutta |
| FR/CPR | Flux Reconstruction/Correction Procedure |
| HPCF | High Performance Computing Facility |
| LE | Leading edge |
| MAV | Micro Aerial Vehicles |
| NACA | National Advisory Committee for Aeronautics |
| NREL | National Renewable Energy Laboratory |
| Re | Reynolds number |
| TE | Trailing edge |
| UAV | Unmanned Aerial Vehicles |
| UMBC | University of Maryland Baltimore County |
| VAWT | Vertical Axis Wind Turbine |
| ZNMF | Zero-net Mass-Flux |

# Chapter 1

# Introduction

## 1.1 Motivation

Since the introduction of boundary layer theory in 1904 by Prandtl [2] and the development of the aeronautics industry, most studies of flow behavior over airfoils have been conducted at high Reynolds numbers. In recent years, however, there has been increasing interest in low Reynolds number applications. Particularly of note are Micro Aerial Vehicles (MAVs) which themselves offer enormous potential: surveillance and reconnaissance operations for the military [3, 4], traffic monitoring and rescue missions for civilians [3], even as a fast and mobile alternative to ground-based rovers for Mars exploration [4]. In this final case, due to the low weight and wing chord length and, considering that its atmosphere is 70 times less dense than Earth's, any martian flight vehicle would be operating at extremely low Reynolds numbers [5]. As figure 1.1 shows, the MAVs, a class of miniature of Unmanned Aerial Vehicles (UAVs), are located in the same Reynolds number regime as small birds and insects.

In an attempt to find solutions for improvements, many researchers have turned to nature for inspiration. For flight improvements at scales with low Re, birds and insects present modifications or adaptations throughout centuries that allowed them to survive many adversities. Birds and insects possess natural wing adaptations to flight at low Reynolds number through slotted wings. In birds, for example, the tip of the slotted feathers moves forward and downward to produce high lift by catching hot vertical columns of air called thermals [7, 8]. MAVs, on the other hand, need mechanisms to improve their ability to fly in a range where viscous forces characterize the flow regime. Contrary to high Reynolds number regimes, where inertial forces characterize the flow, and the transition from laminar to turbulent flow is achieved without disturbance on lift and drag values. However, at low Reynolds number, there are very few studies focused on changes to wing profile to address this issue. Additional concerns regarding this flow regime are that the wing's critical angle of attack is typically at low angle of attack (AoA) and due to the infinity of airfoil models, and that each behaves differently even at the same Re number, studies of individual airfoils need to be done.

This work addresses many of those issues. The NACA 0015 airfoil was chosen due to its

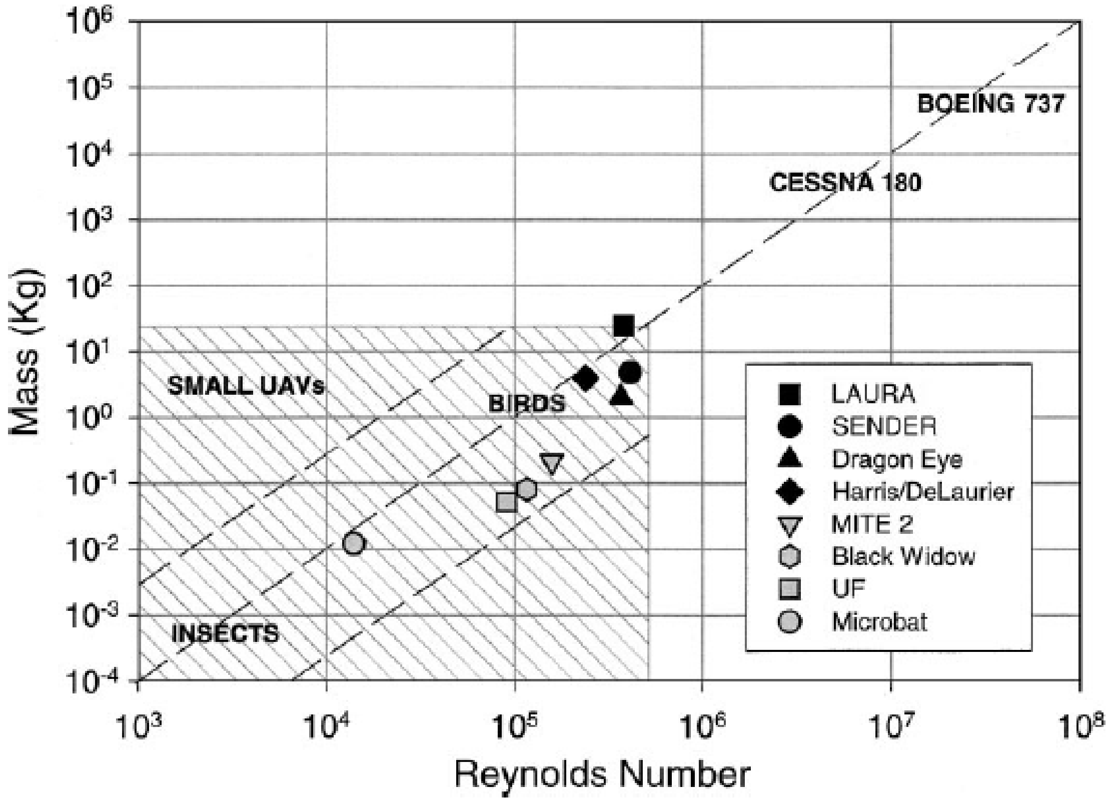


Figure 1.1: Relationship between mass of a flight vehicle and its correspondent Reynolds number [6].

symmetrical shape and simple construction. A passive control design, in this case, internal slot was used in an attempt to see if the slot would delay the angle of attack that the airfoil stalls, and to visualize how the modification affects the boundary layer.

## 1.2 Problem Statement

At low Reynolds number, the flow around an airfoil is laminar and the boundary layer is thicker due to viscous forces. As the flow travels from the leading edge (LE) to the trailing edge (TE), depending on the AoA, the flow can detach from the boundary layer due to adverse pressure. Along the x-direction, at the LE up until the maximum point, pressure goes from high to low meaning that velocity reaches its maximum value at this point. After, pressure starts to increase as it approaches downstream. At the same time, at the wall, the velocity at the boundary layer to fulfill the no-slip condition has to be zero. So, as the flow goes down, the velocity profile along the boundary layer becomes steeper closer to the wall. If the adverse pressure gradient is high enough and flow momentum is low, the flow will be push backwards causing recirculation and laminar flow separation from the surface.

The flow separation from the surface causes stall and each airfoil has a critical AoA, an angle at which the airfoil stalls. As the AoA is increased, the boundary layer goes from fully attached at the LE to slowly becoming thicker and, at the critical AoA, it detaches completely. When it happens, lift values plummet and drag rises by a large factor, deteriorating the airfoil performance. At high Re number, it is possible for the flow to reattach by artificially tripping the boundary layer transition to turbulent flow, but at low Re number, this tripping was not successfully implemented yet [9].

One way to approach this problem is to look for solutions that brings the critical stall angle further up, thus delaying stall from happening. This can be accomplished by flow control solutions. Flow control is divided between active and passive control. The cheapest method would be to modify the geometry in a way that would make the boundary layer attached for longer, this solution constitutes a passive flow control technique.

The focus of this study is to investigate the flow field around an airfoil by means of passive flow control, in this case, with a internal slot at Reynolds number $10^4$ and compare it with the baseline airfoil NACA 0015 to observe if the slot can bring significant input on lift and drag values and if pushes the critical AoA further up.

## 1.3 Outline of Dissertation

In Chapter 2, a literature review on different types of flow control applied to airfoil and wings and its respective study results on the field are described. In Chapter 3, the theory, the CFD (Computational Fluid Dynamics) solver equations and the case set up will be described. In Chapter 4, results and comments will be presented. Chapter 5, study conclusions and suggestions for future work.

# Chapter 2

# Literature Review

Flow control is a category of techniques in engineering by which alterations are made to fluid flows to achieve improvements of some kind (in this review, flow control over airfoils is the primary context). These improvements may include a delay of the laminar-turbulent transition, a postponement of boundary layer separation, an augmentation of turbulent mixing, a suppression of flow induced noise, an enhancement of lift, or a reduction of drag. The impacts of these improvements may take a variety of forms, e.g., improved aerodynamic performance, improved fuel economy, reduced cost, improved regulatory compliance. Flow control techniques can be divided into two categories based on required energy input: active flow control and passive flow control.

## 2.1 Active flow control

Active flow control requires external energy input. This can be achieved through a number of methods. This review covers the following: suction and blowing, zero-net mass-flux, plasma actuators, and acoustic excitation.

### 2.1.1 Suction and blowing

Suction and blowing involve adding or removing fluid to the flow through steady state jets. Suction is the removal of fluid, and is often used to delay boundary layer separation, while blowing is the addition of fluid, and can be used to overcome adverse pressure gradients by increasing the momentum of the flow [10]. Both techniques can modify the pressure distribution over an airfoil surface and lead to dynamic virtual shaping [11]. Suction and blowing effects vary according to their input parameters, which may be amplitude, jet location, and jet angle, all of which can enhance or diminish lift, drag and circulation effects [11]. When used in combination, suction and blowing work better when applied at different locations. Suction is more effective when applied near the leading edge because it manipulates the separation bubble and by reducing the pressure on the suction side, it enhances lift. Additionally, this lower pressure causes flow to remain attached to the surface, decreasing drag. On Huang et al. study [11], blowing was more effective when applied downstream because it manipulates the trailing-edge vortex circulation which improves drag and lift. Figure 2.1 shows an example of suction mechanism.

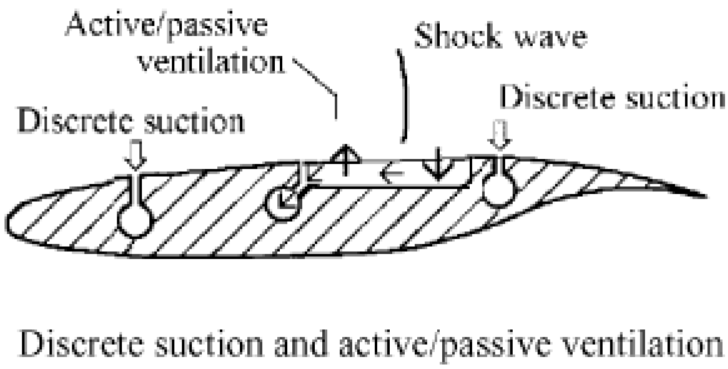


Figure 2.1: Suction flow control mechanism [12].

### 2.1.2 Zero-net Mass-Flux

Zero Net Mass Flux (ZNMF) is similar to suction and blowing, except transient jets are used instead of steady state jets. These jets oscillate between suction and blowing such that the time averaged mass flux is zero, but they still alter the flow by adding significant mean and unsteady momentum to it. The jets themselves are generated by actuators (typically pistons or diaphragms) located in cavities beneath the surface of the airfoil. As they oscillate about their equilibrium positions, they periodically draw fluid into the cavity through an orifice or slot and then expel it back into the flow.

During the blowing stroke, the ejected fluid separates at the sharp edges of the orifice and rolls up to form a vortex pair or a ring. Due to the pressure differential between the ambient flow and the actuator, a sink-like behavior develops, and fluid is drawn back into the actuator. When this occurs, the vortex pair/ring is too far from the orifice to affect the entrainment of fluid back into the cavity. The added unsteady momentum generates vortices that can be used in control and for thrust purposes due to the synthesizing of a time-averaged jet with a finite momentum from the surrounding fluid with zero-net mass transfer during a cycle.

Tuck et al. [13] studied the wall-normal ZNMF located at the leading edge of a NACA 0015 airfoil to find the optimal frequencies that enhance the lift coefficient values. With the optimal frequencies that were determined, the stall angle was mitigated from 10° to 18°, and the lift coefficient exhibited a 46% increase. There was improvement in the lift-to-drag ratio for the range of post-stall angles investigated. Monir et al. [14] compared two different types of synthetic jets: cross boundary-layer and tangential-boundary layer. The inclined angle $a_j$ on the lift enhancement mechanisms of a NACA 23012 airfoil at Reynolds number $2.19x10^6$, and the influence of the blowing ratio $V_j/U_\infty$ were also investigated. The tangential boundary-layer synthetic jet presented considerable stall improvements compared to the cross boundary-layer synthetic jet. At AoA 18°, the lift coefficient was increased by 19.04% and drag coefficient was decreased by 36.19%. The most cost-effective blowing ratio ($V_j/U_\infty$) was three, and, at angle of attack 22°, the absolute maximum $C_l/C_d = 11.19$ occurred when the inclined angle of the jet was $a_j = 0°$.

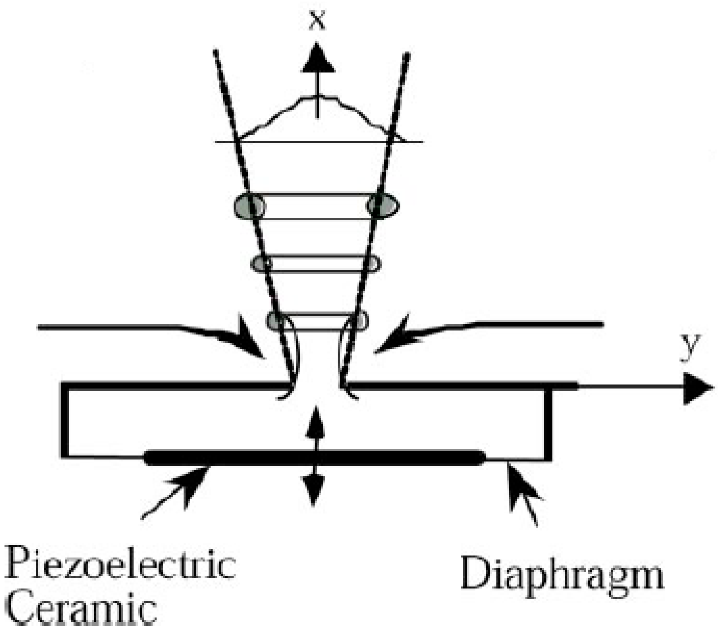


Figure 2.2: Schematic of a synthetic jet actuator [15].

### 2.1.3 Plasma actuators

Plasma actuators are electrical devices that generate a wall bounded jet without the use of any moving parts. Also known as dielectric barrier discharge flow control devices, these actuators consist of two electrodes that are separated by a dielectric material [16]. Figure 2.3 provides an example of how a plasma actuator works.

The most popular variant of non-thermal plasma actuators is the single dielectric barrier discharge actuator. In this variant, one of the electrodes is exposed to the flow surface and the other is fully covered by the dielectric material. A high-voltage AC input is supplied to the electrodes, resulting in an asymmetric electric field in which plasma is produced at voltages above the breakdown voltage $V_B$. Consequently, the air ionizes over the electrode area covered by the dielectric and is accelerated through the electric field [17, 16, 18]. When the plasma actuators are used, the free electrons from the ionized air are repulsed by the upper electrons into two forces. First, the downward thrust force creates a wall jet over the airfoil, which then deflects upward into a spiral vortex that travels from the leading edge down to the trailing edge. As the vortices pass through the upper boundary layer, they bring the free-flowing, high-momentum down by adding momentum to the system, delaying the flow separation, and changing the flow from turbulent to laminar. The second force is ionic thrust in the x-direction down the airfoil. It causes any incoming, free-flowing air to be entrenched in the momentum being forced downwards. As a consequence, all incoming air will be redirected and flow parallel to the airfoil, and with the help of an electromagnetic field after being ionized, it will redirect the crosswind flow and reduce its force on the aircraft.

Vorobiev et al. [19] investigated trailing-edge mounted plasma actuators (SDBDs), for lift enhancement and roll control in a wind tunnel. Two independent, controllable plasma actuators were installed on the left and right suction side of the wing. For the lift enhancement study, $Re = 83,000$ was chosen to describe the results. Based on previous studies, the lift was expected to increase linearly with AoA from $0°$ until $10°$. However, there was a peak at $AoA = 1.5°$ and only on $4° \leq AoA \leq 10°$ did a linear increase occur. The study concluded that the deviations were due to the interaction of the plasma actuators with the viscous flow field, that besides adding momentum to the flow, the actuators affected the flow control by suppressing viscous effect. Both phenomena increased the lift values. The roll control study concluded that the actuators generated constant lift enhancement across the wingspan and the Reynolds number effect showed that lift enhancement by plasma actuators can vary across different low Reynolds numbers.

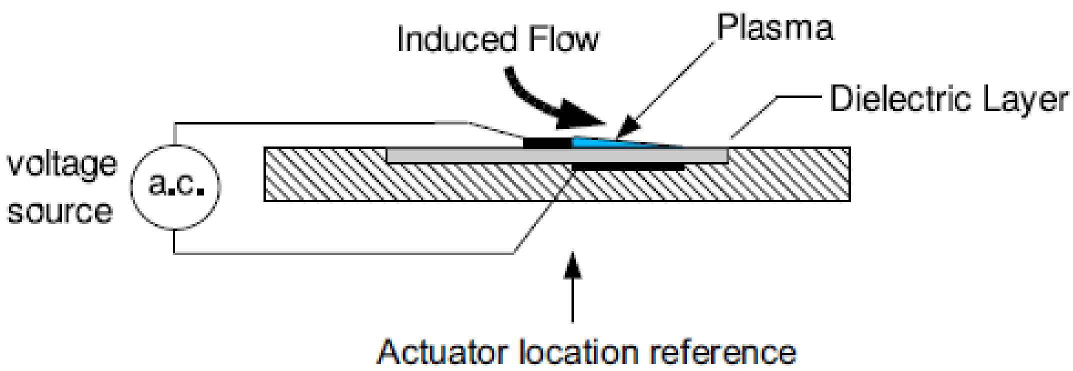


Figure 2.3: Plasma actuator device [16].

### 2.1.4 Acoustic excitation

Acoustic excitation affects the stability of the boundary layer. Small-amplitude excitation in a wide, low-frequency range is found to eliminate laminar separation that otherwise degrades the airfoil performance at low Reynolds number near the design angle of attack. Excitation at high frequencies eliminates pre-stall and periodic shedding of large-scale vortices. Significant improvement in lift is also achieved during post-stall, but with large-amplitude excitation [20]. Yarusevych et al. [21] performed wind tunnel tests to see the effect of external acoustic disturbances on a

NACA 0025 airfoil with a loudspeaker mounted on the test section floor under the leading edge of the airfoil with two types of excitations: one with "pure" acoustic excitation and the other with the help of a speaker to superimpose acoustic excitation with mechanical vibrations. The results showed that both set ups could substantially reduce or suppress the separation region and improve lift and drag values by altering the vortex shedding characteristics. Also, after the separation region was suppressed with a certain amplitude, further increases in amplitude did not change the airfoil performance.

## 2.2 Passive control

In contrast to active flow control, passive flow control requires no energy input. It is often accomplished through the addition of surface features, such as vortex generators, leading-edge tubercles and, internal slots.

### 2.2.1 Vortex generators

Vortex generators are used to prevent or delay flow separation by increasing lift at the expense of slightly increasing drag. Through the geometric addition of small rectangular or delta-shaped protrusions along the wingspan, it energizes the boundary layer ahead of the separation point by transitioning to turbulent flow, thus preventing the flow separation, leading to a pressure drag reduction and improved fight control at lower airspeeds [22, 23]. Bragg et al. [23] tested three different vortex generator designs on a canard airfoil at the 17% and 45% of the chord location (the delta design was only tested at 45% chord location) as a possible solution for the changed in pitch trim reported by Voyager pilots when encountered light rain. As a result of the study, the delta-shaped vortex generators were recommended to be installed to induce drag increase, the aft portion of the wing was smoothed. The pilots reported a better performance regarding cruise speed and an improvement on the elevator stick force. Figure 2.4 shows vortex generators installed in an aircraft wing.

### 2.2.2 Leading-edge tubercles

Leading-edge tubercles are a biomimetic foil design inspired on the flippers of the Humpback whales (*Megaptera novaeangliae*). In Humpback whales, the tubercles are located along the leading edge of the flipper starting approximately at 30% of the flipper span extending until the distal extremity of the flipper [25]. The purpose of the tubercles is to generate vortices by flow excitation to maintain lift. And by keeping the flow attached to the boundary layer, to also prevent stall at high angles of attack [25].

Johari et al.[26] performed water tunnel studies on the aerodynamic effects of a leading edge, modified NACA $63_4$-021 airfoil with tubercles ranging the leading edge protuberance amplitudes and spanwise wavelengths for angle of attacks varying from 6°until 30°. Results showed that compared to the non-modified foil, lift coefficient values of the modified foils on pre-stall regime

Figure 2.4: Vortex generators in an aircraft wing [24].

presented lower values, while in the post-stall regime, it presented values 50% higher. Drag values were higher in the pre-stall regime but independent of the angle of attack in the post-stall regime. The separation flow occurred first in the troughs between adjacent protuberances, and the flow remained attached after the stall angle of attack.

Figure 2.5: Humpback whale (*M.novaeangliae*) flipper [25].

### 2.2.3 Internal slots

Slots are fixed geometrical modifications that allow for a percentage of the fluid flow under the airfoil (pressure side) to travel to the upper side (suction side). This adds momentum to the incoming flow and keeps the flow attached to the airfoil surface. It has the purpose of delaying boundary layer separation by increasing lift values. There are three types of slot configurations: leading-edge, trailing edge, and combined leading and trailing edge.

The leading-edge slot is located at the leading edge and can have different geometrical shapes. Zhang et al. [27] studied leading-edge slots on the upper and bottom surface at the same time with the NACA0015 airfoil for Re 1000, by configuring the geometry using Boolean operations with cutting ellipses and varying the angle of the ellipses from the airfoil chord (figure 2.6). The best inclination angles were the 16° and 17°. Both caused the leading-edge vortices to attach to the surface until they were shed from the trailing edge. The 17° inclination slot compared with the original airfoil design presented a 9.23% power coefficient increase.


Figure 2.6: Leading-edge slots at the upper and bottom surfaces [27].

Belamadi et al. [28] modified a S809 airfoil with a rectangular slot which crossed the upper and lower surfaces. By varying the slot location (X), width (Y) and slope ($\psi$) in search of the optical configuration as shown in figure 2.7. Results showed that the slot position has a significant effect on aerodynamic performance. The best slot location on the upper surface was upstream of the boundary layer separation point. One of Belamadi et al. [28] results demonstrated that by fixing the slot width (Y) at 1.0% of the chord length and slot slope ($\psi$) at $-60\%$ and selecting AoA 18°, the maximum observed lift coefficient was observed at $X = 80\%$ by 3.72% and the drag coefficient for $X = 50\%$ was reduced by 4.8% when compared with baseline values. All together, the slot presence for low angle of attack has no positive effect on the airfoil efficiency, due to the higher overall drag induced by slot flow. Even so, at high AoA, the slot presence increases efficiency by reducing drag and increasing lift values.

With the intent to design an internal slot design capable of simultaneously increasing lift and decreasing drag, Zao Ni [1] designed a tangential internal slot in 2D with two circles of the same radius but offset in the chordwise direction by distance $w$, as shown in figure 2.8. Both circles were tangential to the upper surface (suction side) of the airfoil to effectively guide the flow. The author tested nine different configurations using the NACA $63_4-021$ airfoil. After performing computational simulations at Re $10^5$, the $0.1c\_0.4c$ configuration presented the best maximum

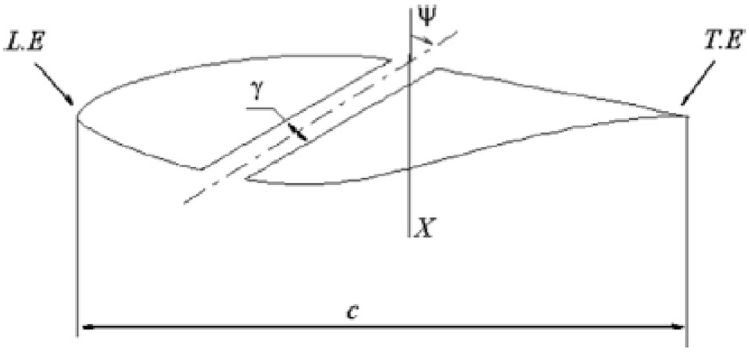


Figure 2.7: Rectangle slot schematics (c: airfoil chord, LE: leading edge, TE: trailing edge, X: slot location, Y: slot width, $\psi$: angle between slot axis and chord normal) [28].

lift-to-drag ratio. Afterwards, this configuration was tested in a water tunnel. Both the simulations and water tunnel results show that for lower AoA ($0 < AoA < 11°$), lift values are low and drag values are high. This is known as "initial loss". Only for $AoA > 11°$, does the slotted airfoil lift-to-drag ratio exceeds the baseline airfoil's by 14%. Zao Ni [1] suggested that this "initial loss" phenomenon could be resolved by adding an active slot mechanism to open or close the slot at appropriate AoAs.

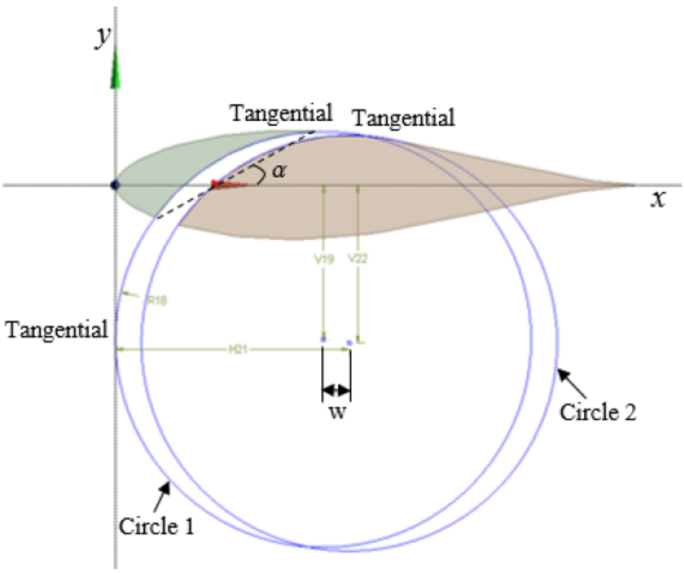


Figure 2.8: Sketch for the internal slot design (c: airfoil chord, w: width of the internal slot, $\alpha$: angle of the internal slot) [1].

A novel two-sided, symmetric slot was developed by Zhu et al. [29] , based on the elliptical hydrofoil from Ribeiro et al. [30] with slots extending from airfoil leading to tailing sections on top and bottom surfaces. With the intent for the semi-active flapping airfoil power generator to extract the fluid power during both the downward and upward flapping, as shown in figure 2.9. Compared to the baseline airfoil, the slotted airfoil improved efficiency by 6.01% and the slot was able to reduce mass and increase the effective lift of the airfoil

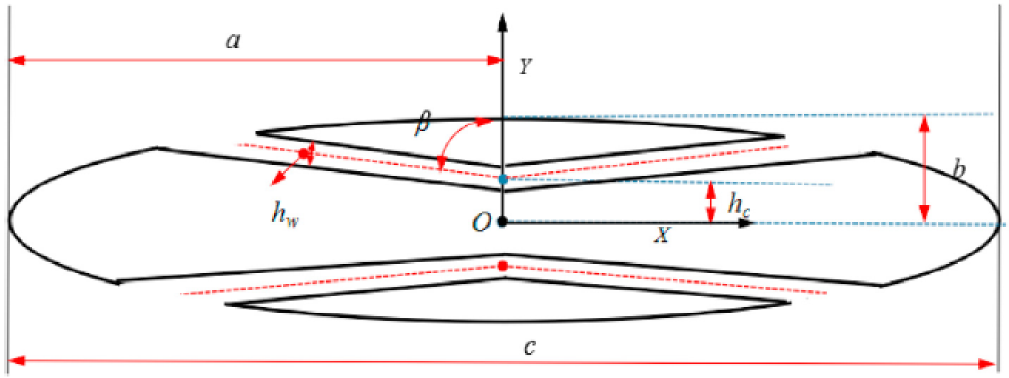


Figure 2.9: The schematic of two-side symmetric slot (a: major axis of the airfoil, b: minor axis of the airfoil, c: airfoil chord, $h_c$: location of the center of the slot from the center of the airfoil, $h_w$: width of the slot, $\beta$: inclination angle of the slot) [29].

An airfoil design with tandem slots was proposed by Mdouki [31] to mitigate or eliminate laminar bubble separation, as shown in fig 2.10. The NREL S809 wind turbine airfoil was the baseline airfoil for the simulations. The tandem slot had a minor effect on pressure distribution near the slots entries and exits but did not impact the overall pressure distribution. Lift and drag values were the same as the baseline airfoil. However, the tandem slot did eliminate the short laminar bubble separation zones on both sides.

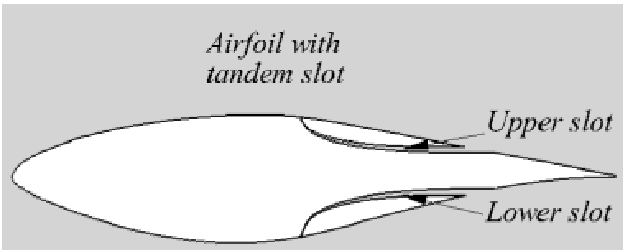


Figure 2.10: NREL S809 airfoil with tandem slot [31].

The trailing-edge slot is located almost at the end of the trailing edge and is known as flap. A flap is a high-lift device that works by increasing the camber of the airfoil and generating maximum lift at lower speed. The camber increase is useful during approaching and landing because it allows the aircraft to descend at a steeper descending angle, thus reducing the distance an aircraft has to begin its descent approach. The maximum lift generation allows the aircraft to lower its required minimum speed [32]. Attie et al. [33] studied the performance optimization of H-type Darrieus

VAWT (Vertical Axis Wind Turbine) by selecting through Design of Experiments, the most likely flap slot trailing edge configurations and performing CFD simulations to obtain the results. The purpose of the flap was to delay early airfoil flow separation and reduce the size of the wake. Results showed that for the optimized flap configuration and, tip speed ratio 3, the wind turbine presented for 2D and 3D models 27% and 19% of power enhancement, respectively. The slotted flapped turbine blades experienced less shedding, which justifies the increased power output. For the turbine blades orientations that the baseline airfoil presented bad results, the slotted flap was able to outperform it, with exception of $\theta = 0°$ and $45°$.

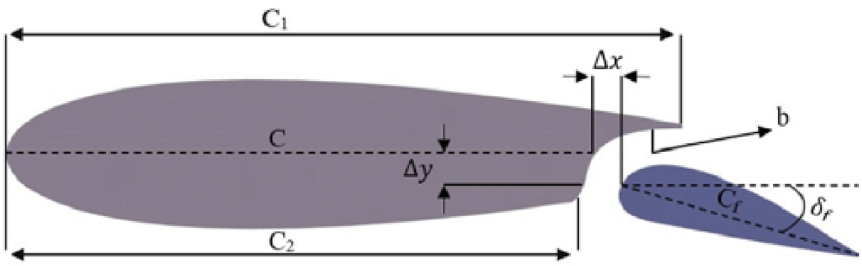


Figure 2.11: Schematic diagram of the single-slotted flapped airfoil [33].

The combined leading and trailing edge configuration blends the aforementioned approaches to reach efficiency and performance in landing and take-off simultaneously. Arra et al [34] in their study they modified the NACA 2412 airfoil by using a combined leading and trailing edge configuration for Re between $10^6$ and $10^7$. By testing different design parameters for the slot and the flap configuration and comparing lift values with AoAs, the authors were able to conclude that the range of lift values lies between 3 and 4 for NACA 2412. The authors did not have any articles to compare their results directly. Figure 2.12 displays the design and the mesh configuration used in the study.

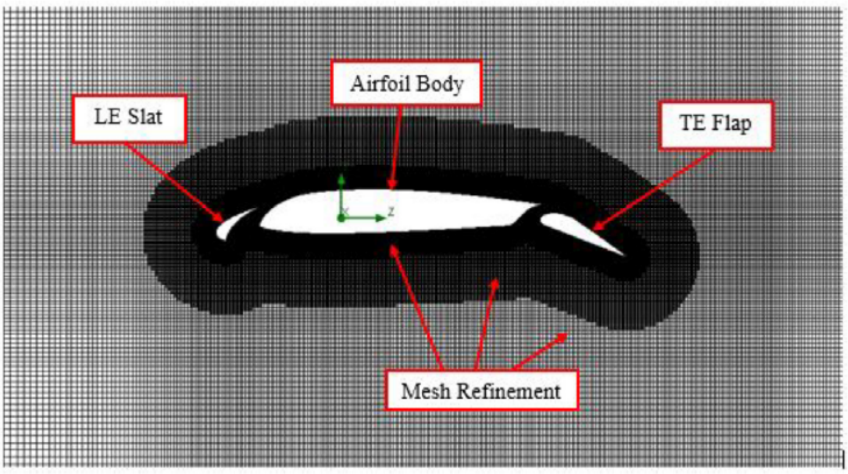


Figure 2.12: Combined leading and trailing-edge configuration [34].

# Chapter 3

# Governing Equations and Computational Setup

The high-order computational fluid dynamics method called flux reconstruction/correction procedure via reconstruction (FR/CPR) is used in this study. Most of the current CFD methods solve the Reynolds averaged Navier-Stokes equations using a first or second-order numerical method together with a turbulence flow model. These low-order methods are fairly accurate, generating results within 5% solution error. However, when considering vortex dominated problems such as flows with large separations, they produce poor results. When this is the case, high-order methods and large eddy simulations are employed [35]. The flux reconstruction/correction procedure (FR/CPR) unifies high-order methods such as the discontinuous Galerkin, spectral difference and spectral volume methods. Below is a descriptive explanation of how the FR/CPR method works. For the mathematical derivations, the reader is invited to consult [36].

For the purposes of explanation, it is helpful to consider the one-dimensional case. The computational domain is discretized into units called cells (simply intervals in 1D). Solutions to the conservation laws are calculated at each of $K$ solution points in each cell. Solution polynomials of order $K-1$ are then formed which interpolate the values at these points. These solve the laws locally, but are discontinuous across cell boundaries. To compensate for these discontinuities, the use of an additional flux function is necessary. To build this function, first, flux values are calculated from the solution values at each of the solution points. Then, a flux polynomial interpolates these flux values, just as the solution polynomials interpolated the solution values. These flux polynomials are, like the solution polynomials, discontinuous between cells but, together, can be thought to constitute a discontinuous flux function over the entire domain. The next step is to make it continuous. First, a common value must be assigned at the cell boundaries. In all cases, this will be the flux value from the upwind cell. Next, a correction function will be applied which approximates the zero function, but whose value at the left boundary of the cell is equal to the magnitude of the jump. This will achieve continuity.

To extend this method to two/three dimensions, the idea is to transform the governing equations from a physical element to the reference or standard element and then apply the 1D CPR formulation on the standard element in each coordinate direction. Figure 3.1 shows the solutions points expanded to 2D.

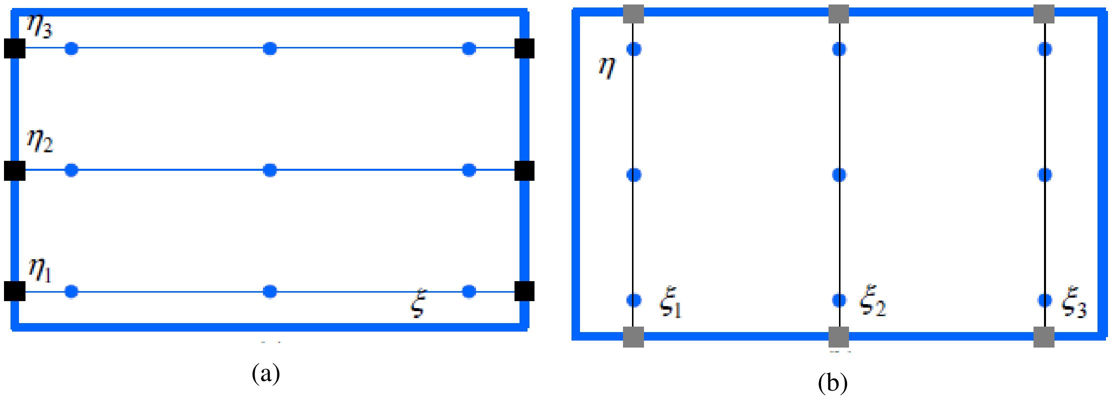


Figure 3.1: **(a) Solution points (dots) and flux points on vertical boundaries (squares).** *At each of theses flux points, we define an upwind flux value* $f_{upw}$. **(b) Flux points on horizontal boundaries (squares)**. *Here, we define* $g_{upw}$ [36].

Previous studies [37, 38, 39, 40] have shown that these methods are accurate and applicable to the type of problem in the current research.

## 3.1 Governing Equations

The governing equations for unsteady compressible Navier-Stokes flow are used in this study and is express in the conservative form as

$$\frac{\partial Q}{\partial t} + \frac{\partial F}{\partial x} + \frac{\partial G}{\partial y} + \frac{\partial H}{\partial z} = 0 \tag{3.1}$$

where $Q = (\rho, \rho u, \rho v, \rho w, E)^T$ are conservative variables, $\rho$ is the fluid density, $u$, $v$ and $w$ are flow velocities in the x-, y- and z-directions, and $E$ is the total energy given by $E = \frac{p}{\gamma - 1} + \frac{1}{2}\rho(u^2 + v^2 + w^2)$ for a perfect gas in which $p$ is the pressure and $\gamma$ is the constant specific heat capacity ratio. The total energy formula closes the solution system. $F, G$ and $H$ are total flux vectors including the inviscid and viscous flux terms in the x-, y- and z-direction, respectively, which are expressed as

$$F = F^i - F^v = \left\{ \begin{array}{c} \rho u \\ \rho u^2 + p - \tau_{xx} \\ \rho v u - \tau_{xy} \\ \rho w u - \tau_{xz} \\ u(E+p) - u\tau_{xx} - v\tau_{xy} - w\tau_{xz} - \frac{\mu C_p}{Pr} T_x \end{array} \right\},$$

$$G = G^i - G^v = \begin{Bmatrix} \rho v \\ \rho uv - \tau_{yx} \\ \rho v^2 + p - \tau_{yy} \\ \rho wv - \tau_{yz} \\ v(E+p) - u\tau_{yx} - v\tau_{yy} - w\tau_{yz} - \frac{\mu C_p}{Pr} T_y \end{Bmatrix},$$

$$H = H^i - H^v = \begin{Bmatrix} \rho w \\ \rho uw - \tau_{zx} \\ \rho vw - \tau_{zy} \\ \rho w^2 + p - \tau_{zz} \\ w(E+p) - u\tau_{zx} - v\tau_{zy} - w\tau_{zz} - \frac{\mu C_p}{Pr} T_z \end{Bmatrix},$$

where $\mu$ is the dynamic viscosity, $C_p$ is the specific heat at constant pressure, $P_r$ is the Prandtl number and $T$ is the temperature. For the Newtonian fluids, the viscous stresses are given as follows:

$$\begin{aligned} \tau_{xx} &= 2\mu\left(u_x - \frac{u_x + v_y + w_z}{3}\right) \\ \tau_{yy} &= 2\mu\left(v_y - \frac{u_x + v_y + w_z}{3}\right) \\ \tau_{zz} &= 2\mu\left(w_z - \frac{u_x + v_y + w_z}{3}\right) \\ \tau_{xy} &= \tau_{yx} = \mu\left(v_x + u_y\right) \\ \tau_{xz} &= \tau_{zx} = \mu\left(w_x + u_z\right) \\ \tau_{yz} &= \tau_{zy} = \mu\left(w_y + v_z\right) \end{aligned}$$

To facilitate numerical simulation, the governing equation (3.1) in the physical domain $(t,x,y,z)$ is transformed into computational domain $(\tau,\xi,\eta,\zeta)$ as shown in figure 3.2. Eq. (3.1) can be written as follows:

$$\frac{\partial \tilde{Q}}{\partial \tau} + \frac{\partial \tilde{F}}{\partial \xi} + \frac{\partial \tilde{G}}{\partial \eta} + \frac{\partial \tilde{H}}{\partial \zeta} = 0, \tag{3.2}$$

where,

$$\begin{cases} \tilde{Q} = |J|Q \\ \tilde{F} = |J|(Q\xi_\tau + F\xi_x + G\xi_y + H\xi_z) \\ \tilde{G} = |J|(Q\eta_\tau + F\eta_x + G\eta_y + H\eta_z) \\ \tilde{H} = |J|(Q\zeta_\tau + F\zeta_x + G\zeta_y + H\zeta_z) \end{cases} \tag{3.3}$$

Note that in the coordinate transformation, $\tau = t$ and $(\xi,\eta,\zeta) \in [-1,1]\times[-1,1]\times[-1,1]$ is a standard element in computational domain. The Jacobian matrix of the coordinate transformation

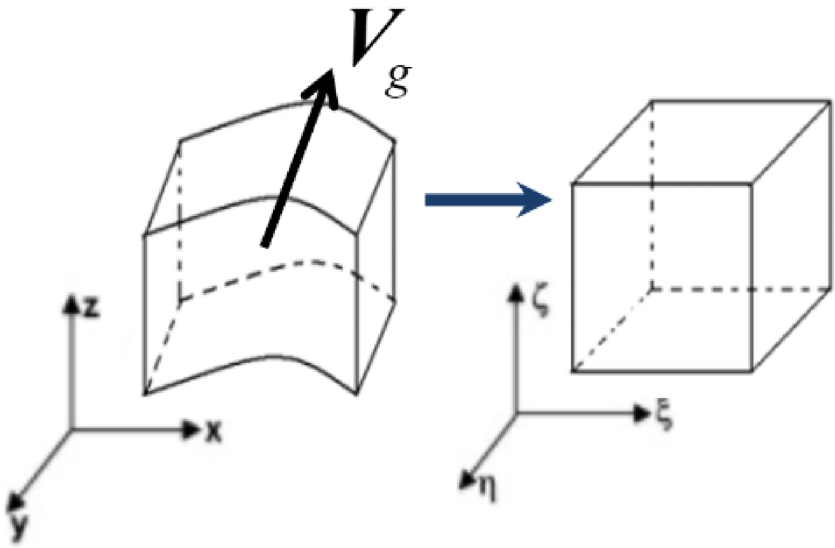


Figure 3.2: Transformation from a moving physical domain to a fixed computational domain [41].

can be written as the following form:

$$J = \frac{\partial(x,y,z,t)}{\partial(\xi,\eta,\zeta,\tau)} = \begin{pmatrix} x_\xi & x_\eta & x_\zeta & x_\tau \\ y_\xi & y_\eta & y_\zeta & y_\tau \\ z_\xi & z_\eta & z_\zeta & z_\tau \\ 0 & 0 & 0 & 1 \end{pmatrix} \tag{3.4}$$

The inverse transformation must also exist for a non-singular transformation. Therefore, the inverse of the Jacobian matrix can be written as:

$$J^{-1} = \frac{\partial(\xi,\eta,\zeta,\tau)}{\partial(x,y,z,t)} = \begin{pmatrix} \xi_x & \xi_y & \xi_z & \xi_t \\ \eta_x & \eta_y & \eta_z & \eta_t \\ \zeta_x & \zeta_y & \zeta_z & \zeta_t \\ 0 & 0 & 0 & 1 \end{pmatrix} \tag{3.5}$$

The metrics $\xi_t, \eta_t$ and $\zeta_t$ are related to the grid velocity vector $\vec{v}_{grid}$ as

$$\left\{ \begin{array}{l} \xi_t = -\vec{v}_{grid} \cdot \nabla \xi, \\ \eta_t = -\vec{v}_{grid} \cdot \nabla \eta, \\ \zeta_t = -\vec{v}_{grid} \cdot \nabla \zeta, \end{array} \right. \tag{3.6}$$

The geometric conservation law has been enforced following the error compensation approach [42].

### 3.1.1 Spatial Discretization and time Integration Methods

The Flux Reconstruction/Correction Procedure via Reconstruction (FR/CPR) [37, 43, 38, 40, 36, 44, 45] method was used to solve the governing equations. A brief introduction of the FR/CPR method is discussed in this section for the sake of completeness, but a full discussion of the method can be found in [37]. In FR/CPR methods, the flux terms in Eq. (3.2) are divided into two parts, i.e. local fluxes $\tilde{F}^{loc}$ constructed from local solutions and correction fluxes $\tilde{F}^{cor}$ by mapping the differences between the local fluxes and the common fluxes on the element interfaces into the entire element with high-order correction functions. This can be expressed as:

$$\begin{cases} \tilde{F}(\xi,\eta,\zeta) = \tilde{F}^{loc}(\xi,\eta,\zeta) + \tilde{F}^{cor}(\xi,\eta,\zeta) \\ \tilde{G}(\xi,\eta,\zeta) = \tilde{G}^{loc}(\xi,\eta,\zeta) + \tilde{G}^{cor}(\xi,\eta,\zeta) \\ \tilde{H}(\xi,\eta,\zeta) = \tilde{H}^{loc}(\xi,\eta,\zeta) + \tilde{H}^{cor}(\xi,\eta,\zeta) \end{cases} \tag{3.7}$$

On substituting Eq. (3.7) into Eq. (3.2), the governing equations in the computational domain can be reformulated as:

$$\frac{\partial \tilde{Q}}{\partial \tau} + \left( \frac{\partial \tilde{F}^{loc}}{\partial \xi} + \frac{\partial \tilde{G}^{loc}}{\partial \eta} + \frac{\partial \tilde{H}^{loc}}{\partial \zeta} \right) + \left( \frac{\partial \tilde{F}^{cor}}{\partial \xi} + \frac{\partial \tilde{G}^{cor}}{\partial \eta} + \frac{\partial \tilde{H}^{cor}}{\partial \zeta} \right) = 0 \tag{3.8}$$

In this study, the inviscid common fluxes on the element interfaces were calculated using Roe approximate Riemann solver [46] and the common viscous fluxes were obtained by the second approach (BR2) developed by Bassi and Rebay [47]. To minimize numerical errors when performing simulations on curved elements [48], Eq. (3.8) can be transformed back to the physical domain as

$$\frac{\partial Q}{\partial \tau} + \left( \frac{\partial F^{loc}}{\partial \xi} + \frac{\partial G^{loc}}{\partial \eta} + \frac{\partial H^{loc}}{\partial \zeta} \right) + \delta^{cor} - \vec{v}_{grid} \cdot \nabla Q = 0 \tag{3.9}$$

To solve Eq. (3.9), it can be rewritten as

$$\frac{\partial Q}{\partial \tau} = R(Q, \nabla Q), \tag{3.10}$$

For the 2D simulations with moving grid, a third-order accurate spatial discretization, sixth-stage forth-order explicit singly diagonally implicit Runge-Kutta (ESDIRK) method [38, 45] was used in the simulations with time-steps of $10^{-4}$ and $10^{-3}$. The general formulation of ESDIRK is written as

$$\begin{cases} Q^{n+1} = Q^n + \Delta t \sum_{i=1}^{s} b_i R(Q_i), \\ Q_i = Q^n + \Delta t \sum_{j=1}^{i} a_{ij} R(Q_j), \quad i = 1, \ldots s, \end{cases} \tag{3.11}$$

where $s$ is the number of stages and

$$a_{ii} = \begin{cases} 0, & i = 1 \\ w, & i \neq 1 \end{cases} \tag{3.12}$$

Equation (3.11) can be written as

$$\begin{cases} Q^{n+1} = Q^n + \Delta t \sum_{i=1}^{s} b_i R(Q_i), \\ Q_1 = Q_n, \\ Q^i = \Delta t \omega R(Q_i) + Q^n + \Delta t \sum_{j=1}^{i-1} a_{ij} R(Q_j), \quad i = 2, \dots s, \end{cases} \tag{3.13}$$

## 3.2 Computational setup

The NACA 0015 airfoil was selected for the study of low Reynolds number flow dynamics at Re number $10^4$ and for the modified slotted airfoil. The design for the slotted airfoil was based on the work of Zao Ni [1]. The optimal design parameters found by him was applied on a NACA 0015 airfoil, as is shown in figure 3.3. Both circles have the same radius of $0.4c$ and have to be tangent to the upper surface of the airfoil. One of the circles is offset from the center by a width $w = 0.10c$ and the one located more to the left has also to be tangent to the y axis.

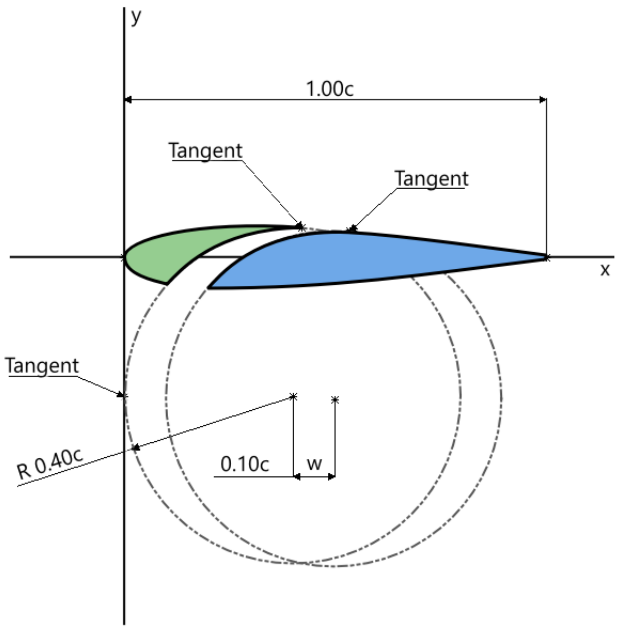


Figure 3.3: Slot design and parameters of NACA 0015 airfoil.

The 2D computational domain was designed to simulate the flow across the airfoil. The simulation domain comprises of two different shape domains, a rectangular domain, figure 3.4a, resembling a wind tunnel test section (far from the airfoil) and a C-grid domain, figure 3.4b, to better capture the airfoil leading-edge curvature (close to the airfoil). The rectangular domain has a width of $100c$ and total length of $151c$. Figure 3.4 shows the domain dimensions based on the airfoil chord length.

For this study the airfoil chord length is $c = 1$. The boundary conditions at the inlet was set as inflow velocity, at top and bottom surfaces as symmetric, the outlet was set as outflow and,

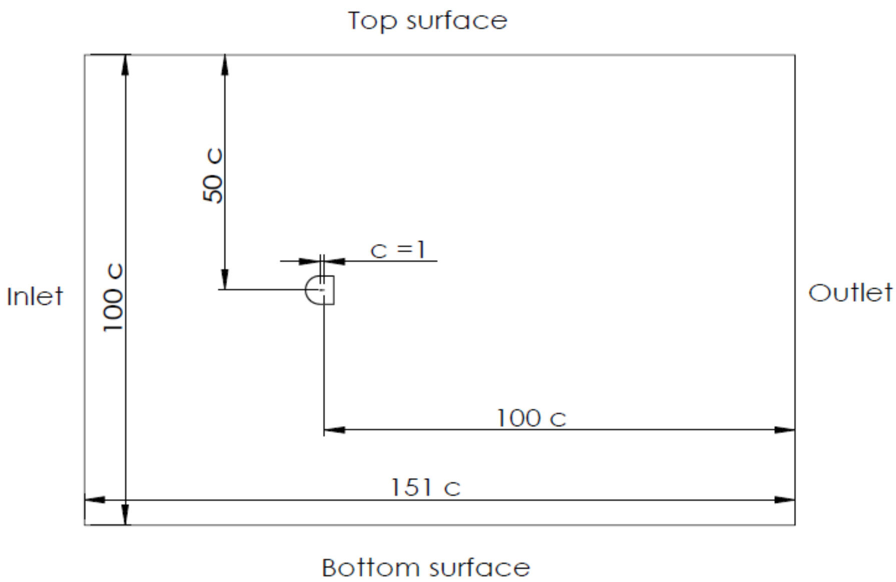


(a) Rectangle domain.

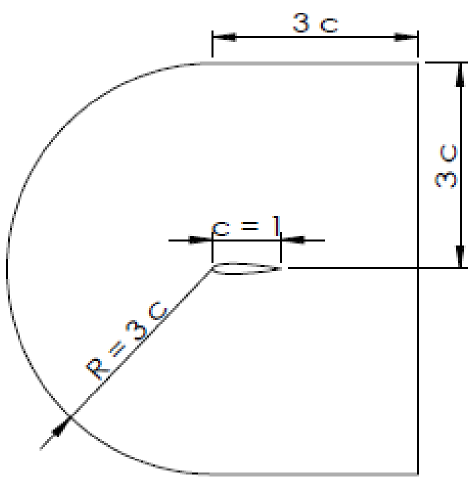


(b) Detail view of the C-shaped domain.

Figure 3.4: Schematics of the computational domain.

at the airfoil wall, a wall function. The computational domain for the baseline NACA 0015 and for the slotted design have 37920 and 17169 unstructured quadrilateral elements respectively. To satisfy the wall function at the airfoil wall, the y+ value was set to $y^+ = 0.6$. The CFD simulations considered air as the fluid and Mach number of $Ma = 0.1$. Figure 3.5 shows the meshes for the baseline airfoil and the slotted airfoil.

All the simulations were performed on the high performance computing facility of the University of Maryland, Baltimore County (UMBC) with the UMBC in-house code.

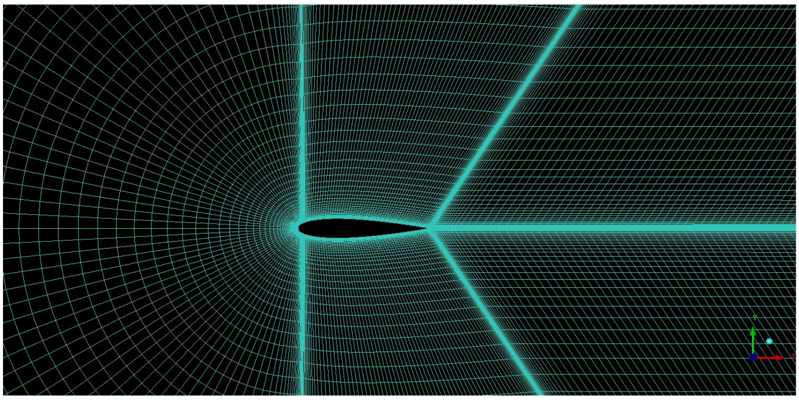

(a) original design

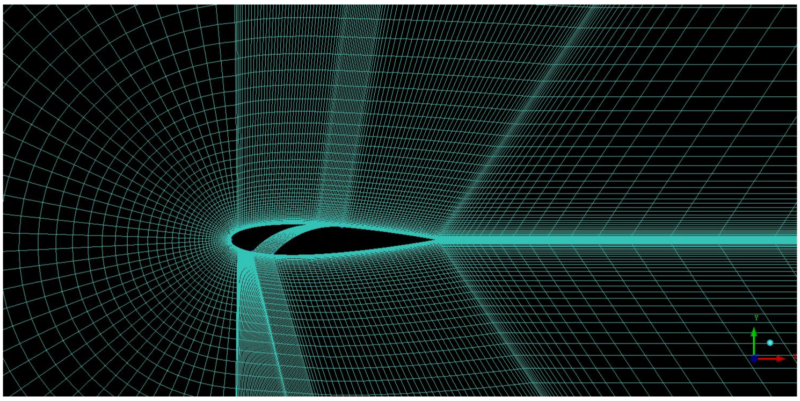

(b) slotted design

Figure 3.5: NACA 0015 mesh domains. (a) original design; (b) slotted design.

# Chapter 4

# Results

To understand the effect of the slot on the performance of the airfoil, the NACA 0015 airfoil and the slotted design were simulated for $8 \leq AoA \leq 24^{\circ}$, where the main coefficients, lift and drag were calculated and analysed. To calculate the lift and drag coefficients, eq. (4.1) and eq. (4.2) were considered for 2D airfoil, in which $F_x$ and $F_y$ are respectively the horizontal force (drag) and the vertical force (lift) measured per unit length, $V_{\infty}$ is the freestream velocity and $c$ is the chord length.

$$C_D = \frac{F_x}{0.5\rho U_{\infty} c} \tag{4.1}$$

$$C_L = \frac{F_y}{0.5\rho U_{\infty} c} \tag{4.2}$$

The vorticity z plots for AoAs $8^{\circ}, 10^{\circ}$and $12^{\circ}$ are shown in figure 4.1, for $14^{\circ}, 16^{\circ}$and $18^{\circ}$ are shown in figure 4.2, and for $20^{\circ}, 22^{\circ}$and $24^{\circ}$ are shown in figure 4.3. The original airfoil results are displayed on the left and the slotted design on the right. It is noticeable that for the same AoA, for the baseline airfoil, the flow displays chaotic behavior on the suction side while for the slotted airfoil, the flow exhibits a more controlled behavior. This can be further observed in figures 4.4, figure 4.5, and figure 4.6 presenting the lift and drag coefficients. The baseline plots present significant amplitude variations on lift coefficient values when compared with those of the slotted design. Even at high AoA, the slotted design presents less variation on the lift coefficient amplitude over time.

This is due to the internal slot. First, by adding momentum from the pressure to the suction side, it makes the flow less unsteady for all the AoA tested by keeping the incoming vortices spinning on the surface towards the trailing edge. Second, by splitting the airfoil into two smaller airfoils, the flow detached from the left airfoil can be energised by the flow detached from the right airfoil, which also brings the flow to roll over the remaining airfoil surface.

Beginning at the AoA $8^{\circ}$, the flow coming from the bottom surface through the slot flows downstream along with the incoming flow from the leading edge. Until AoA $11^{\circ}$, the slotted configuration add instability to the flow, hence it does not provide lift similar to the baseline model. This phenomena is known as initial loss and it can be seen at figure 4.7c, where the slotted $Cl/Cd$ values, start presenting higher values than the baseline airfoil. Until this AoA, it is not worth it to use the slotted airfoil, as the baseline one presents better results. Further increase in the AoA, the flow through the slot changes its behavior and, at the top surface, part of it rolls counterclockwise (yellow color) towards the LE and the remaining goes downstream. The flow coming from the LE, presents negative vorticity z values, so it rolls clockwise. Combined, these two movements make the flow roll in and out of the top surface, providing the slotted design with stable lift and drag values for a longer range of AoAs. In figure 4.3d and figure 4.3f, the flow in front of the downstream wall of the slot detaches from the LE and it joins part of the flow coming from the airfoil and it helps keep the flow attached to the surface.

12° (figure 4.1e) is the critical stall angle for NACA 0015 airfoil and the flow detached for the first time at the LE at $t = 31s$ (figure 4.4e). However, the slotted airfoil does not stall at this AoA. Only at AoA 18° the slotted airfoil's lift values decreased (figure 4.5f), meaning it reached stall. The slotted mitigated the stall angle from 12° to 18°. At post-stall angles, contrary to the baseline airfoil, the slotted airfoil due to the internal slot, presents less variation on Cl and Cd values along the run and this can be seen in all plots on the right side in figures 4.4. 4.5, and 4.6.

The vortices movement in and out of the upper surface, cannot be characterized as a reattachment of the boundary layer. Ohtake et al. [49], in his wind tunnel experiment with NACA 0012 airfoil at Re 10,000, concluded that the flow does not reattach. Further studies need to be done for the slotted design to confirm or refute Ohtake et al. statement.

Figure 4.7 display the lift and drag coefficient for all the simulated AoA. Comparing figure 4.7a and figure 4.7b, the baseline airfoil for most of the runs presented higher lift and drag coefficient values when compared to the slotted design. This behavior indicates that its performance is not especially efficient. In aerodynamics, it is desired for most of the applications to have high lift values while the drag values remain small. In figure 4.7c, It can be seem that, after its initial loss interval, the slotted design performs better than the baseline post-stall angles. At 14°, it presents the highest lift over drag ratio with 5.38 and, at 22°, it presents its maximum efficiency compared with the baseline by 74%.

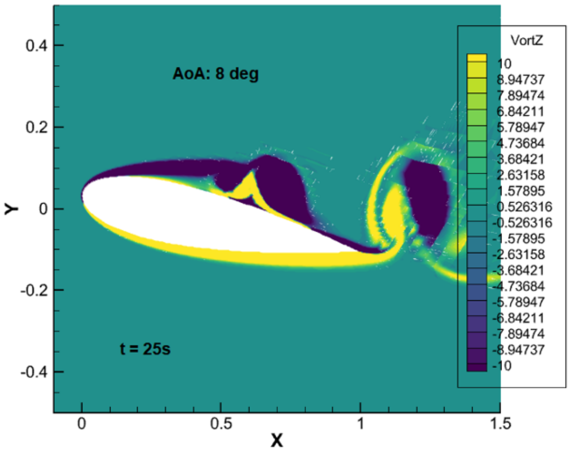


(a) 8° baseline

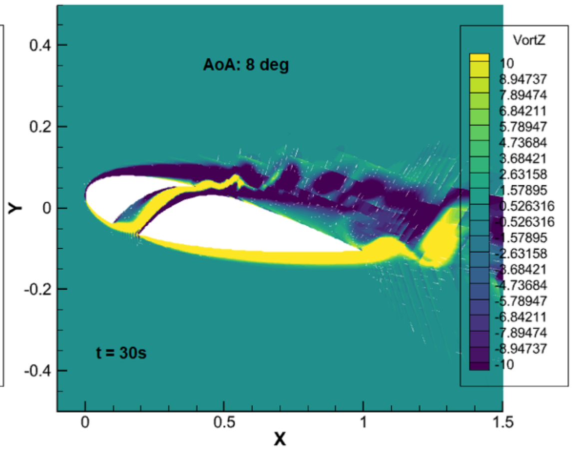


(b) 8° slotted

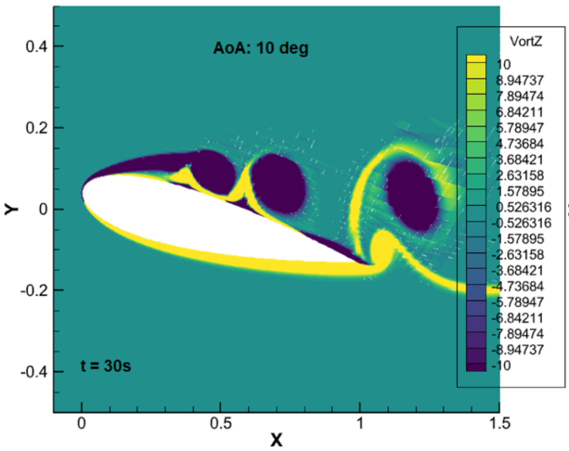


(c) 10° baseline

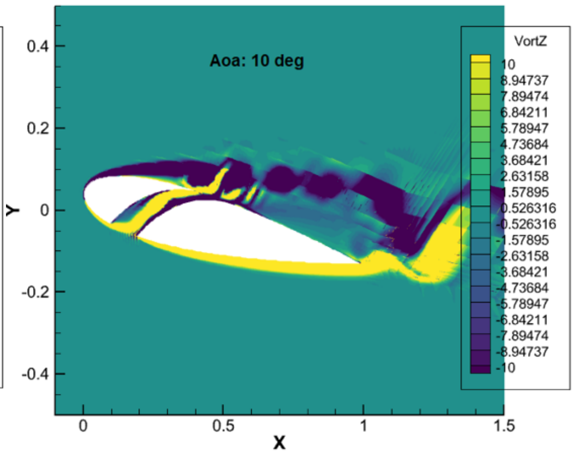


(d) 10° slotted

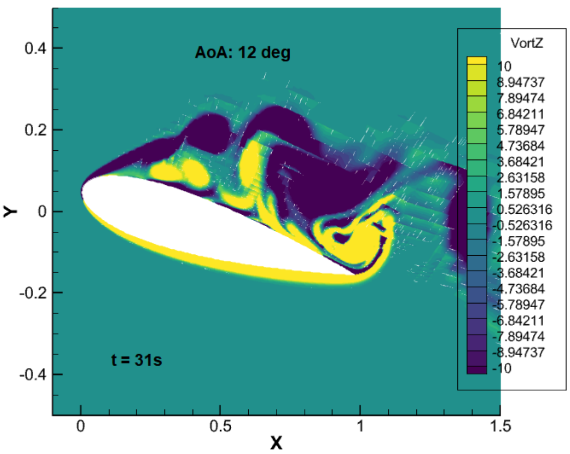


(e) 12° baseline

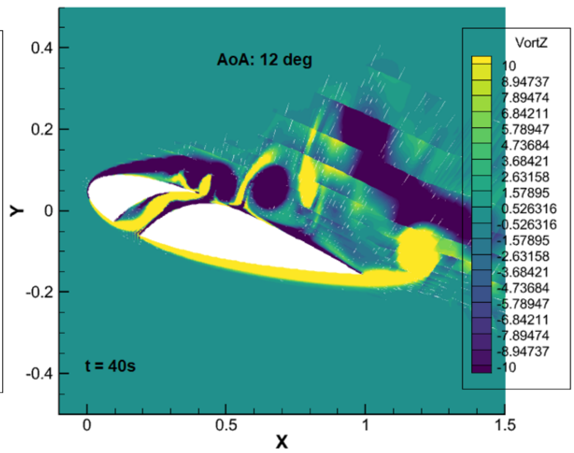


(f) 12° slotted

Figure 4.1: Vorticity z plots for 8°, 10° and 12°.

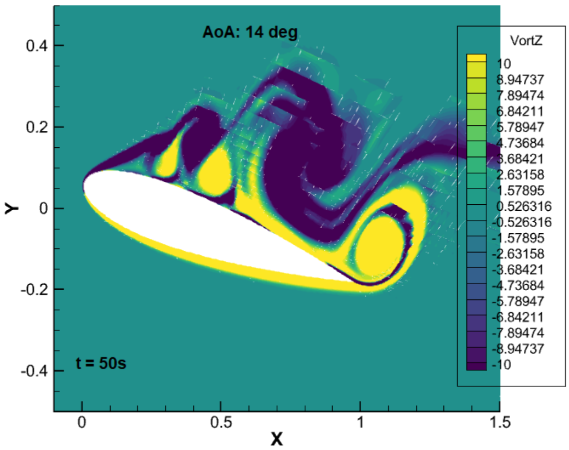


(a) 14° baseline

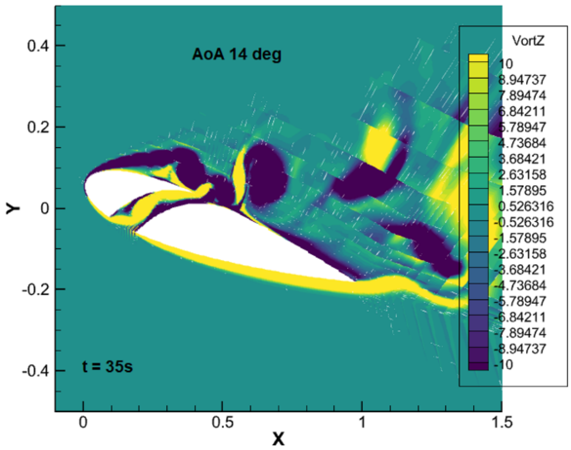


(b) 14° slotted

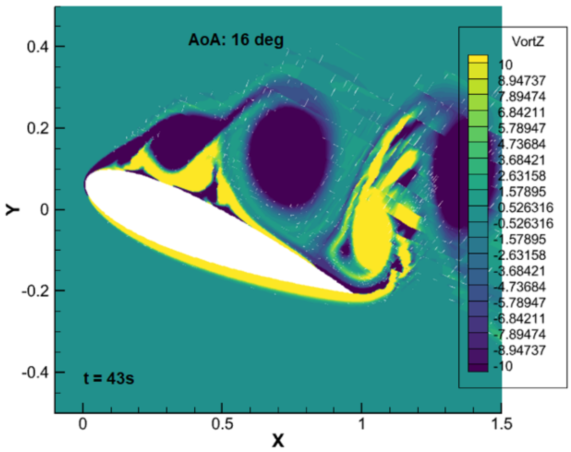


(c) 16° baseline

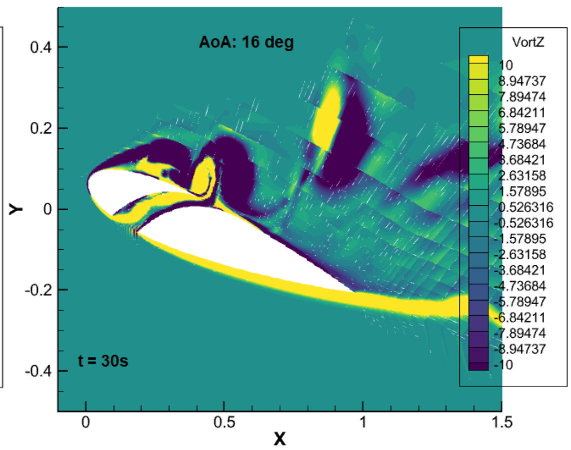


(d) 16° slotted

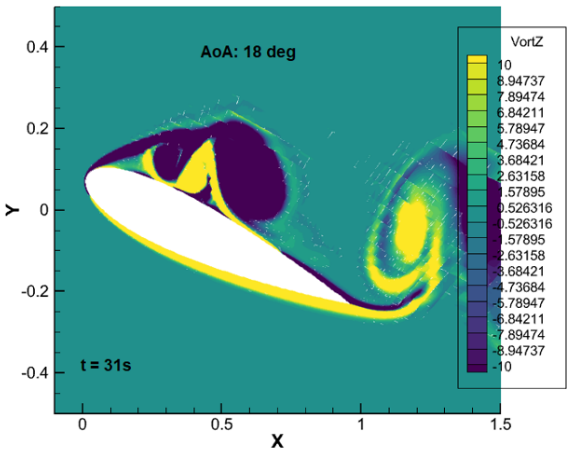


(e) 18° baseline

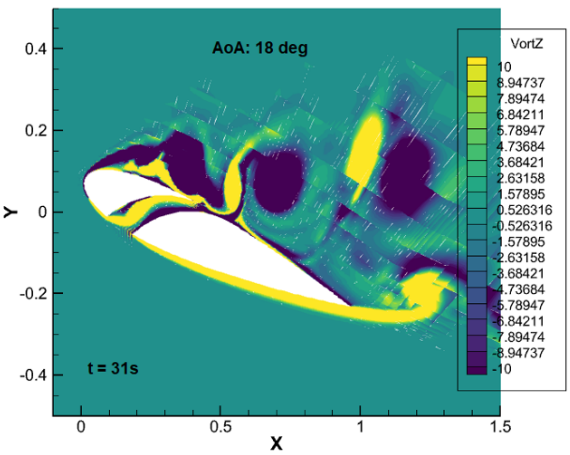


(f) 18° slotted

Figure 4.2: Vorticity z plots for $14^\circ, 16^\circ$ and $18^\circ$.

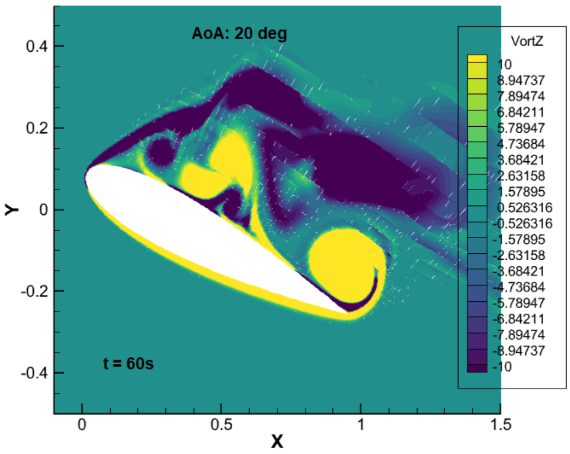


(a) 20° baseline

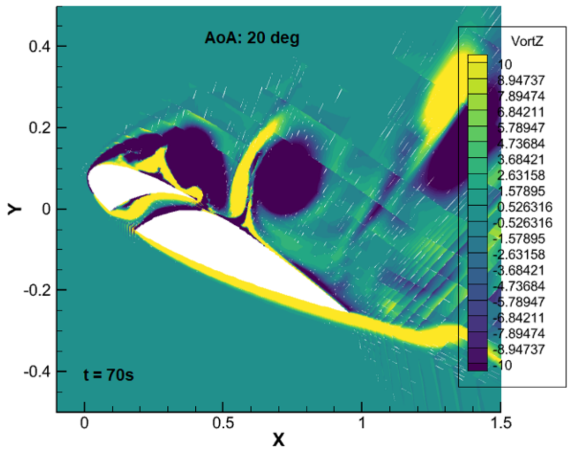


(b) 20° slotted

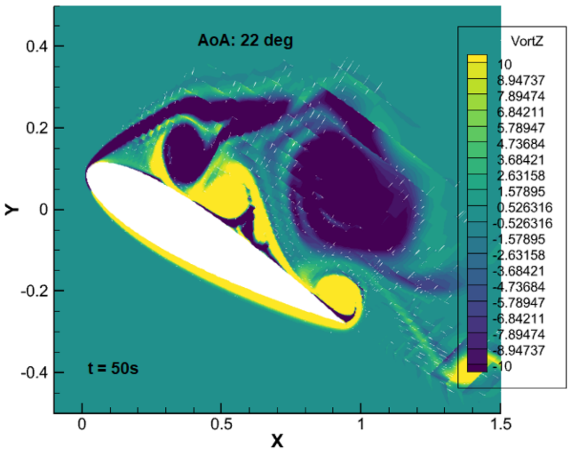


(c) 22° baseline

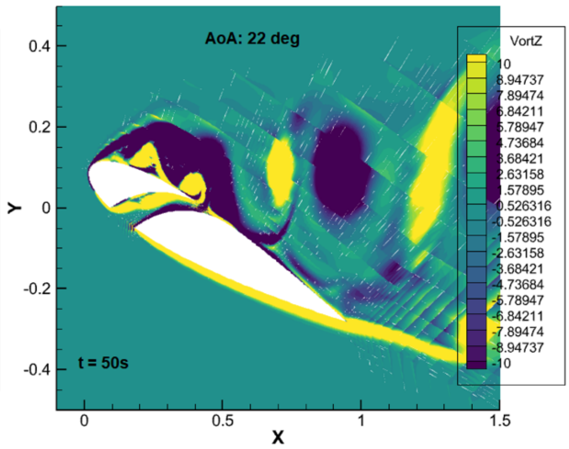


(d) 22° slotted

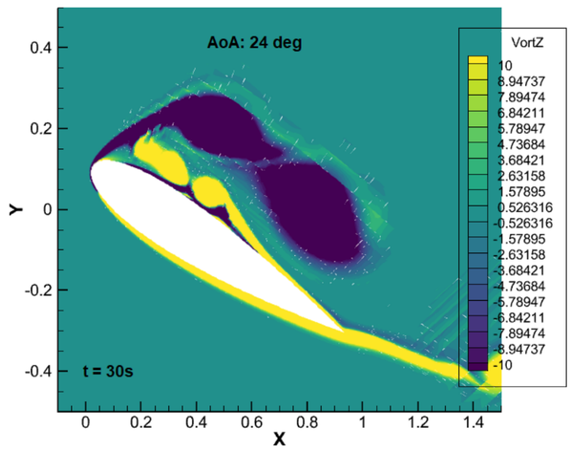


(e) 24° baseline

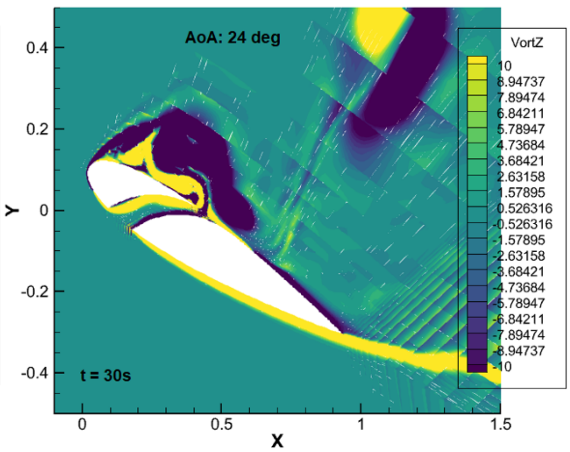


(f) 24° slotted

Figure 4.3: Vorticity z plots for 20°, 22° and 24°

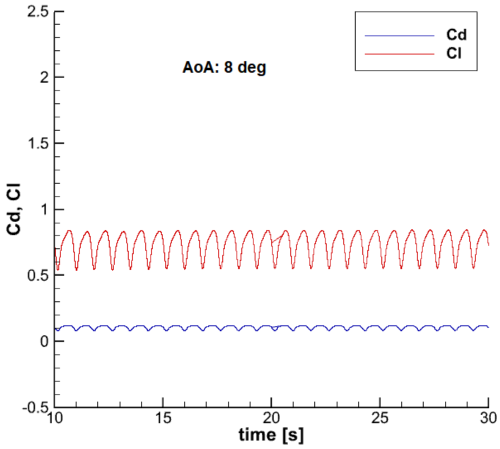


(a) 8° baseline

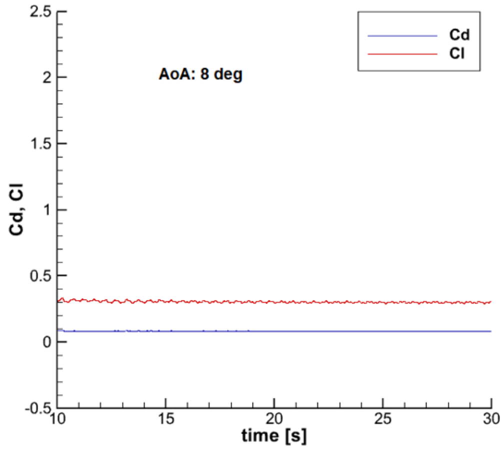


(b) 8° slotted

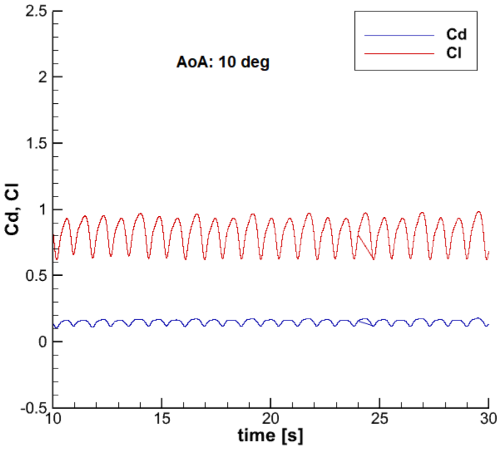


(c) 10° baseline

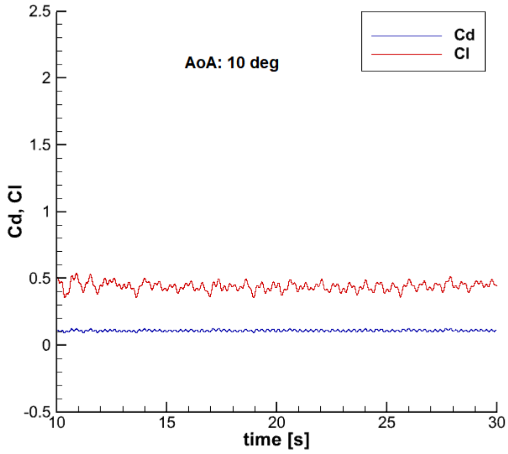


(d) 10° slotted

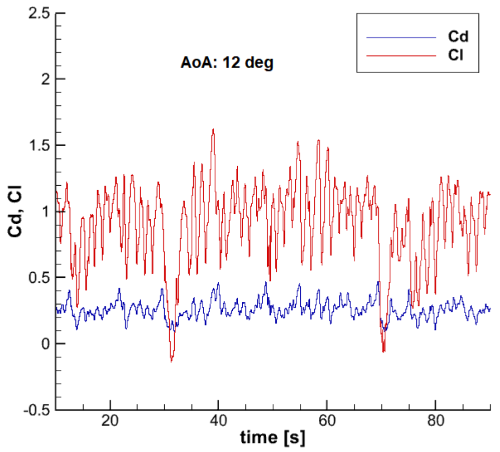


(e) 12° baseline

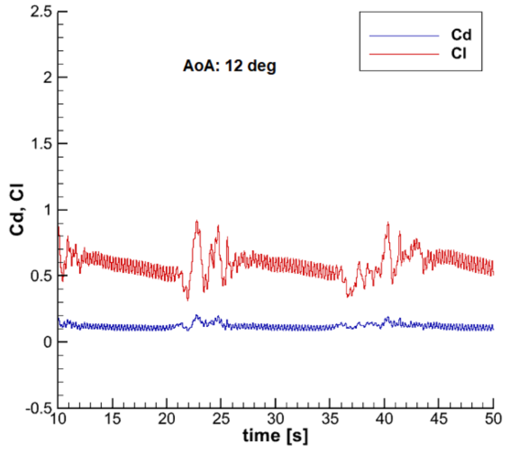


(f) 12° slotted

Figure 4.4: Cd, Cl x time plots for 8°, 10° and 12°.

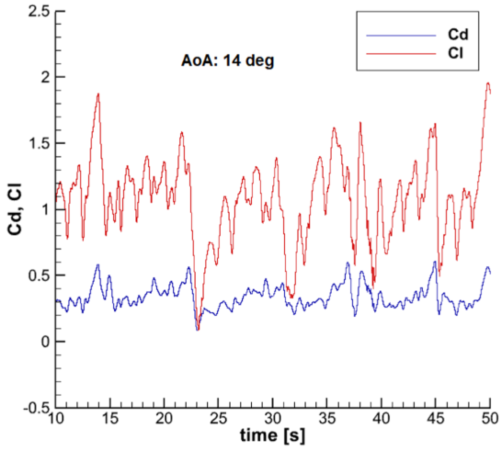


(a) 14° baseline

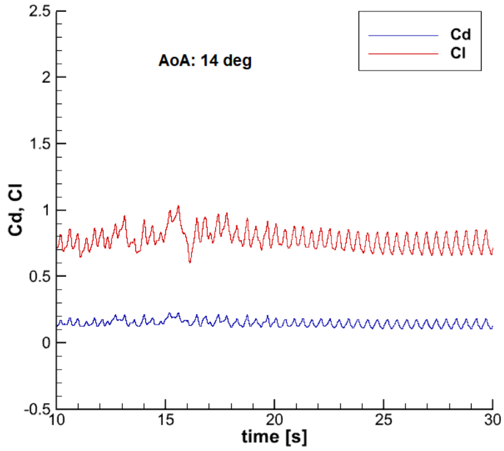


(b) 14° slotted

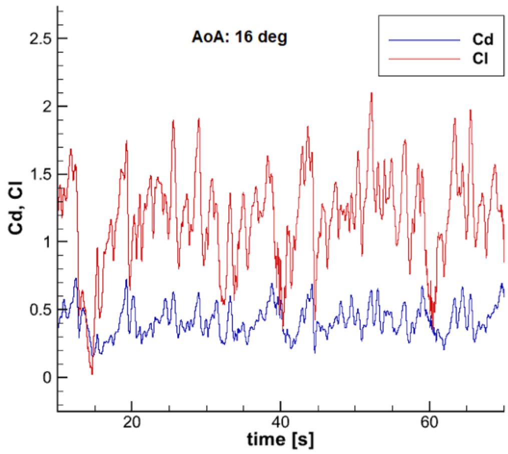


(c) 16° baseline

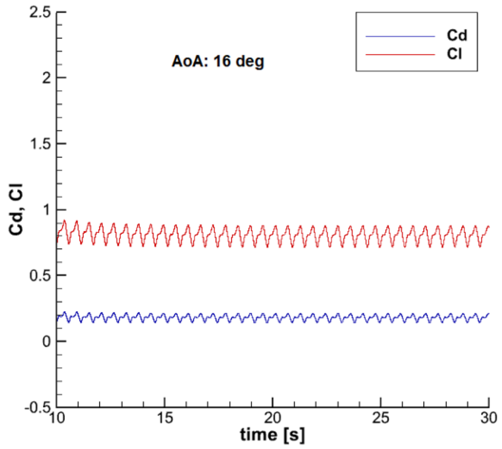


(d) 16° slotted

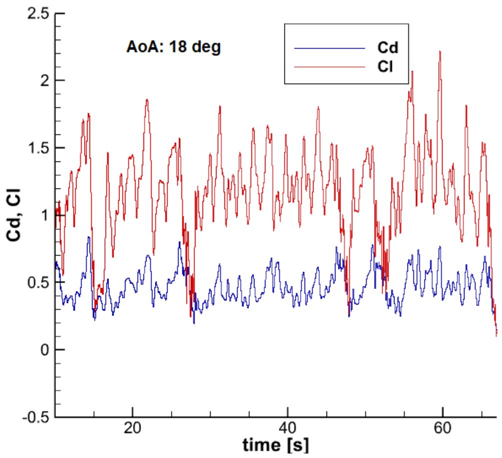


(e) 18° baseline

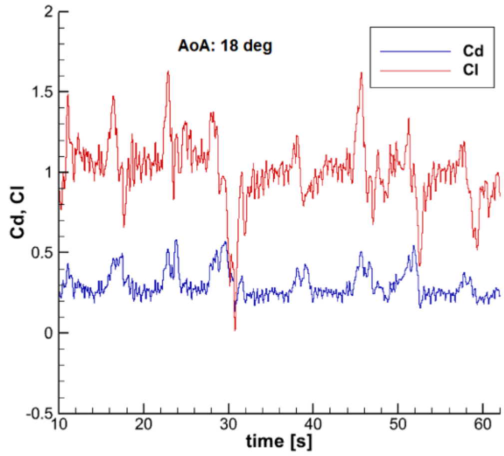


(f) 18° slotted

Figure 4.5: Cd, Cl x time plots for 14°, 16° and 18°.

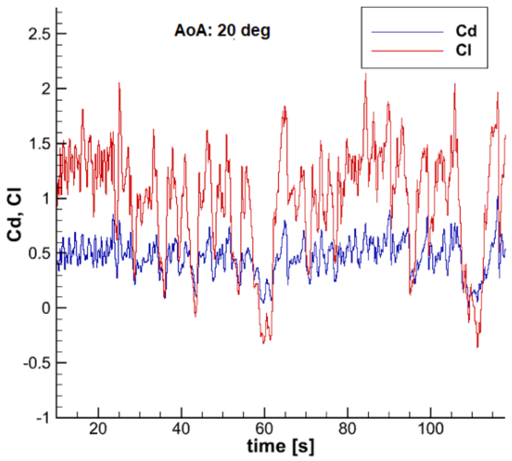


(a) 20° baseline

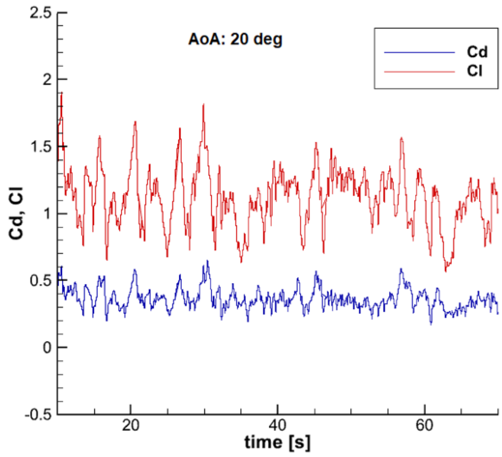


(b) 20° slotted

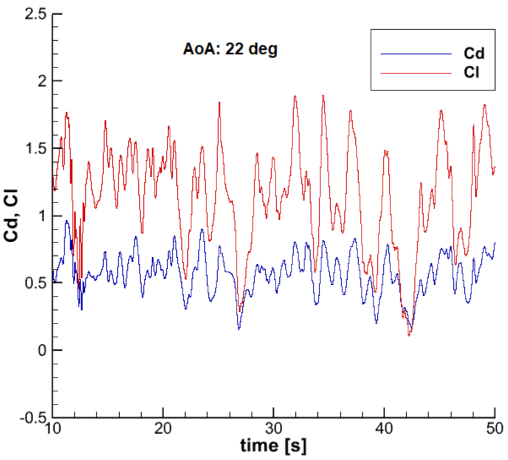


(c) 22° baseline

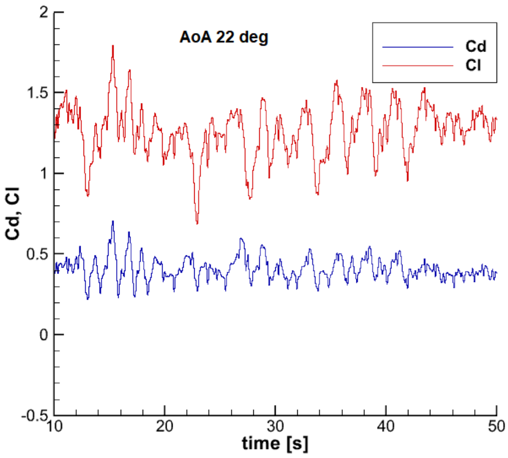


(d) 22° slotted

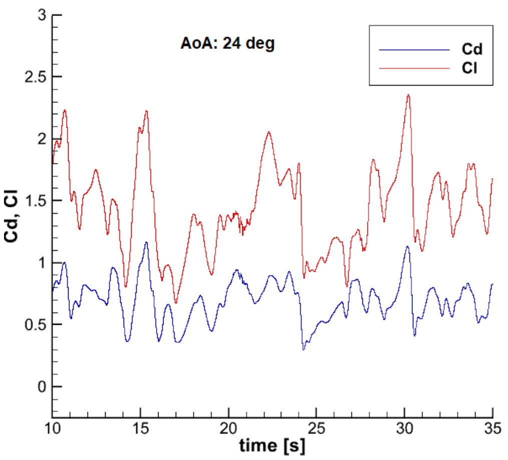


(e) 24° baseline

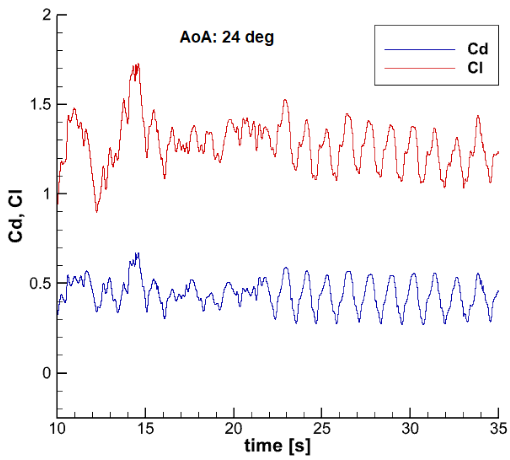


(f) 24° slotted

Figure 4.6: Cd, Cl x time plots for 20°, 22° and 24°.

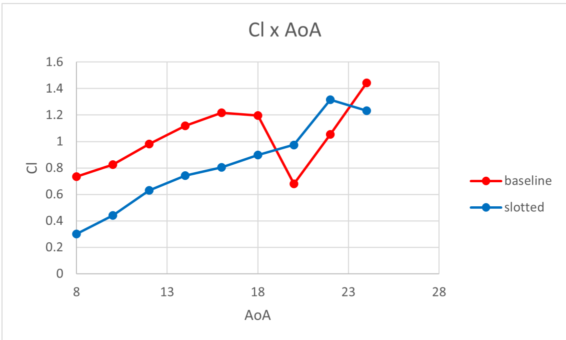


(a) Cl x AoA.

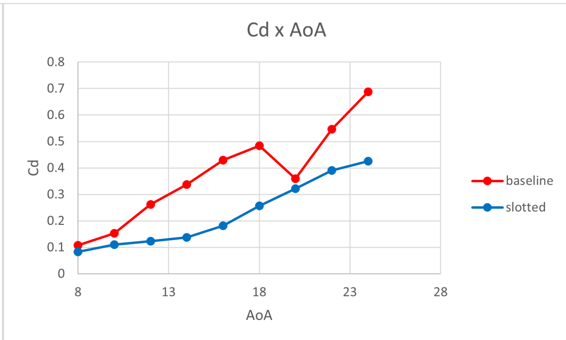


(b) Cd x AoA.

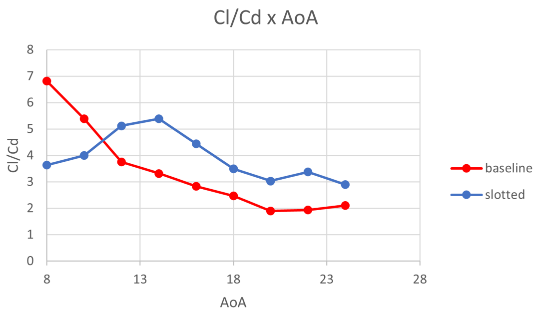


(c) Cl/Cd x AoA.

Figure 4.7: Lift and drag coefficient values x AoA plots for the complete simulations.

# Chapter 5

# Conclusions and Future Work

This dissertation came to fulfill the increased interest in low Reynolds number fluid behavior, by performing CFD simulations on a NACA 0015 airfoil and a modified design with an internal slot to study how the internal slot would impact the flow behavior around the airfoil.

Results showed that the slotted design delays the laminar flow separation, thus increasing the stall angle from $12^\circ$ to $18^\circ$. However, for AoA less than $11^\circ$, the slotted design performs worse than the unmodified airfoil. This phenomena is known as initial loss and for AoA smaller than $11^\circ$, it is better not to use the slotted design. In 3D, this problem would be solved by keeping the slats closed. Slats are the internal slot applied in a spanwise direction that can be open or closed as required.

Regarding the flow behavior, the slotted design presented less unsteady movements with smaller variations in lift and drag amplitude values due to the vortices rolling in and out of the the top surface. This behavior cannot be characterized as a reattachment of the boundary layer. Further studies are needed to make a final statement.

Considering the lift-to-drag ratio, above $11^\circ$, the slotted design presented better results, even at post-stall AoA. On a smaller note, Zao Ni's [1] design parameters that originally was tested on a NACA $63_4 21$ and in this study was applied on a NACA 0015 presented remarkable results, even when both airfoils presented different shape.

It can be concluded that the slotted airfoil has potential for further applications in low Reynolds number regimes and present a feasible option in minimizing the viscous characteristics of the laminar separation flow.

In future work, verification and validation of the results are necessary. As a step further, pitch the slotted airfoil up and down to study dynamic stall behavior. This would be closer to real life maneuvers encountered by MAVs. 3D simulations to observe the slotted design effect in the spanwise direction and perform wind tunnel experiments to verify if the differences in results are significant and if further modifications are necessary to adapt this solution to a full 3D model.

# Bibliography


[1] Zao Ni, *Flow Control Through Geometric Modifications to Improve Airfoil/Hydrofoil Performance*. PhD thesis, Florida Atlantic University, 2019.

[2] L. Prandtl, "Über Flüssigkeits-bewegungen bei sehr kleiner Reibung.," in *Verhandlinger II Int. Math.- Kongr.*, (Heidelberg. Leipzig), pp. 484–494, 1904.

[3] G. Flores, S. Zhou, R. Lozano, and P. Castillo, "A Vision and GPS-Based Real-Time Trajectory Planning for a MAV in Unknown and Low-Sunlight Environments," *Journal of Intelligent & Robotic Systems*, vol. 74, pp. 59–67, apr 2014.

[4] J. Winslow, H. Otsuka, B. Govindarajan, and I. Chopra, "Basic Understanding of Airfoil Characteristics at Low Reynolds Numbers (104–105)," *Journal of Aircraft*, vol. 55, pp. 1050–1061, may 2018.

[5] R. Shrestha, M. Benedict, V. Hrishikeshavan, and I. Chopra, "Hover Performance of a Small-Scale Helicopter Rotor for Flying on Mars," *Journal of Aircraft*, vol. 53, pp. 1160–1167, jul 2016.

[6] T. J. Mueller and J. D. DeLaurier, "Aerodynamics of Small Vehicles," *Annual Review of Fluid Mechanics*, vol. 35, pp. 89–111, jan 2003.

[7] R. P. Holland, "Birds Have Natural Slotted Wings," *Scientific American*, vol. 143, pp. 386–388, nov 1930.

[8] The CornellLab of Ornithology, "Birds and their Wing Shapes." https://www.birds.cornell.edu/k12/wp-content/uploads/2018/11/Bird-Wing-Types-Handout.pdf.

[9] B. H. Carmichael, "Low Reynolds number airfoil survey, volume 1," tech. rep., NASA, 1982.

[10] T. Moghaddam and N. B. Neishabouri, "On the Active and Passive Flow Separation Control Techniques over Airfoils," *IOP Conference Series: Materials Science and Engineering*, vol. 248, p. 012009, oct 2017.

[11] L. Huang, P. G. Huang, R. P. LeBeau, and T. Hauser, "Numerical Study of Blowing and Suction Control Mechanism on NACA0012 Airfoil," *Journal of Aircraft*, vol. 41, pp. 1005–1013, sep 2004.

[12] E. Stanewsky, "Adaptive wing and flow control technology," *Progress in Aerospace Sciences*, vol. 37, pp. 583–667, oct 2001.

[13] A. Tuck and J. Soria, "Active Flow Control over a NACA 0015 Airfoil using a ZNMF Jet," in *15th Australasian Fluid Mechanics Conference*, no. December, pp. 1–4, 2004.

[14] H. Esmaeili Monir, M. Tadjfar, and A. Bakhtian, "Tangential synthetic jets for separation control," *Journal of Fluids and Structures*, vol. 45, pp. 50–65, feb 2014.

[15] A. Glezer and M. Amitay, "Synthetic Jets," *Annual Review of Fluid Mechanics*, vol. 34, pp. 503–529, jan 2002.

[16] T. C. Corke, M. L. Post, and D. M. Orlov, "SDBD plasma enhanced aerodynamics: concepts, optimization and applications," *Progress in Aerospace Sciences*, vol. 43, pp. 193–217, oct 2007.

[17] R. D. Joslin, D. N. Miller, and F. K. Lu, *Fundamentals and Applications of Modern Flow Control Edited by ASTRONAUTICS AND AERONAUTICS*. American Institute of Aeronautics and Astronautics, Inc., 2009.

[18] Foodsystems Lab, "Cold Plasma Actuator to Reduce Crosswind Force on Aircraft Tailfin," 2021. https://www.youtube.com/watch?v=8uSO3c4UgeU.

[19] A. N. Vorobiev, R. M. Rennie, E. J. Jumper, and T. E. McLaughlin, "Experimental Investigation of Lift Enhancement and Roll Control Using Plasma Actuators," *Journal of Aircraft*, vol. 45, pp. 1315–1321, jul 2008.

[20] K. B. M. Q. Zaman, A. Bar-Sever, and S. M. Mangalam, "Effect of acoustic excitation on the flow over a low- Re airfoil," *Journal of Fluid Mechanics*, vol. 182, p. 127, sep 1987.

[21] S. Yarusevych, J. G. Kawall, and P. E. Sullivan, "Effect of Acoustic Excitation on Airfoil Performance at Low Reynolds Numbers," *AIAA Journal*, vol. 41, pp. 1599–1601, aug 2003.

[22] T. H. C. O. C. A. D. Karakoc, ed., *New Frontiers in Sustainable Aviation*. Springer, 2022.

[23] M. B. Bragg and G. M. Gregorek, "Experimental study of airfoil performance with vortex generators," *Journal of Aircraft*, vol. 24, pp. 305–309, may 1987.

[24] J. W. Tallman, "What Am I? Vortex Generators," 2017. https://www.aopa.org/news-and-media/all-news/2017/august/flight-training-magazine/vortex-generators.

[25] F. E. Fish, L. E. Howle, and M. M. Murray, "Hydrodynamic flow control in marine mammals," *Integrative and Comparative Biology*, vol. 48, pp. 788–800, apr 2008.

[26] H. Johari, C. Henoch, D. Custodio, and A. Levshin, "Effects of Leading-Edge Protuberances on Airfoil Performance," *AIAA Journal*, vol. 45, pp. 2634–2642, nov 2007.

[27] J. Zhang, Y. Yan, P. Xie, L. Jiang, and J. Zhu, "Effect of leading-edge slot on energy capture performance of semi-active flapping airfoil," *Energy Reports*, vol. 8, pp. 5225–5234, nov 2022.

[28] R. Belamadi, A. Djemili, A. Ilinca, and R. Mdouki, "Aerodynamic performance analysis of slotted airfoils for application to wind turbine blades," *Journal of Wind Engineering and Industrial Aerodynamics*, vol. 151, pp. 79–99, apr 2016.

[29] J. Zhu, M. Zhu, T. Zhang, H. Zhao, and C. Wang, "Improvement of the power extraction performance of a semi-active flapping airfoil by employing two-sided symmetric slot airfoil," *Energy*, vol. 227, jul 2021.

[30] B. L. R. Ribeiro, S. L. Frank, and J. A. Franck, "Vortex dynamics and Reynolds number effects of an oscillating hydrofoil in energy harvesting mode," *Journal of Fluids and Structures*, vol. 94, p. 102888, apr 2020.

[31] R. Mdouki, "Passive Control of Laminar Bubble Separation for S809 Wind Turbine Airfoil via Slot," in *23ème Congrès Français de Mécanique*, 2017.

[32] "Flap (aeronautics)." https://en.wikipedia.org/wiki/Flap_(aeronautics).

[33] C. Attie, A. ElCheikh, J. Nader, and M. Elkhoury, "Performance enhancement of a vertical axis wind turbine using a slotted deflective flap at the trailing edge," *Energy Conversion and Management*, vol. 273, p. 116388, dec 2022.

[34] A. Arra, N. Anekar, and S. Nimbalkar, "Aerodynamic effects of leading edge (LE) slats and slotted trailing edge (TE) flaps on NACA-2412 airfoil in prospect of optimization," *Materials Today: Proceedings*, vol. 44, pp. 587–595, 2021.

[35] Z. J. WANG and H. T. HUYNH, "A review of flux reconstruction or correction procedure via reconstruction method for the Navier-Stokes equations," *Mechanical Engineering Reviews*, vol. 3, no. 1, pp. 15–00475–15–00475, 2016.

[36] H. T. Huynh, "A Flux Reconstruction Approach to High-Order Schemes Including Discontinuous Galerkin Methods," in *18th AIAA Computational Fluid Dynamics Conference*, (Reston, Virigina), American Institute of Aeronautics and Astronautics, jun 2007.

[37] M. Yu and L. Wang, "A high-order flux reconstruction/correction procedure via reconstruction formulation for unsteady incompressible flow on unstructured moving grids," *Computers & Fluids*, vol. 139, pp. 161–173, nov 2016.

[38] L. Wang and M. Yu, "Comparison of ROW, ESDIRK, and BDF2 for Unsteady Flows with the High-Order Flux Reconstruction Formulation," *Journal of Scientific Computing*, vol. 83, p. 39, may 2020.

[39] L. Wang and M. Yu, "An implicit high-order preconditioned flux reconstruction method for low-Mach-number flow simulation with dynamic meshes," *International Journal for Numerical Methods in Fluids*, vol. 91, pp. 348–366, nov 2019.

[40] L. Wang and M. Yu, "On the parallel implementation and performance study of high-order Rosenbrock-type implicit Runge-Kutta methods for the FR/CPR solutions of the Navier-Stokes equations," in *2018 AIAA Aerospace Sciences Meeting*, no. January, (Reston, Virginia), pp. 1–18, American Institute of Aeronautics and Astronautics, jan 2018.

[41] N. Poudel, *Analysis of Stationary and Flapping Wings in Unsteady Flow Environments at Low Reynolds*. PhD thesis, University of Maryland Baltimore County (UMBC), 2022.

[42] M. Yu, Z. Wang, and H. Hu, "A high-order spectral difference method for unstructured dynamic grids," *Computers & Fluids*, vol. 48, pp. 84–97, sep 2011.

[43] Z. Wang and H. Gao, "A unifying lifting collocation penalty formulation including the discontinuous Galerkin, spectral volume/difference methods for conservation laws on mixed grids," *Journal of Computational Physics*, vol. 228, pp. 8161–8186, nov 2009.

[44] P. E. Vincent, P. Castonguay, and A. Jameson, "A New Class of High-Order Energy Stable Flux Reconstruction Schemes," *Journal of Scientific Computing*, vol. 47, pp. 50–72, apr 2011.

[45] L. Wang and M. Yu, "Jacobian-free implicit p-adaptive high-order compact direct flux reconstruction methods for unsteady flow simulation," in *AIAA Aviation 2019 Forum*, (Reston, Virginia), p. p. 3062, American Institute of Aeronautics and Astronautics, jun 2019.

[46] P. Roe, "Approximate Riemann solvers, parameter vectors, and difference schemes," *Journal of Computational Physics*, vol. 43, pp. 357–372, oct 1981.

[47] F. Bassi, A. Crivellini, S. Rebay, and M. Savini, "Discontinuous Galerkin solution of the Reynolds-averaged Navier–Stokes and k–$\omega$ turbulence model equations," *Computers & Fluids*, vol. 34, pp. 507–540, May 2005.

[48] M. Yu, Z. Wang, and Y. Liu, "On the accuracy and efficiency of discontinuous Galerkin, spectral difference and correction procedure via reconstruction methods," *Journal of Computational Physics*, vol. 259, pp. 70–95, feb 2014.

[49] T. Ohtake and Y. Sakai, "Characteristics of unsteady flow field of laminar separation bubble on a NACA 0012 airfoil at low Reynolds numbers," *18th International Symposium on Flow Visualization*, 2018.